



# Assessing built microclimate with building group frontal projection maps: A sun-path-dependent deep transfer learning neural network approach

Qi Li<sup>a</sup>, Wei Wang<sup>b</sup>, Xiaowei Luo<sup>a</sup>, Jiayu Chen<sup>c,\*</sup>

<sup>a</sup> Department of Architecture and Civil Engineering, City University of Hong Kong, Kowloon, Hong Kong

<sup>b</sup> School of Architecture, Southeast University, Nanjing, China

<sup>c</sup> School of Civil Engineering, Tsinghua University, Beijing, China



## ARTICLE INFO

### Keywords:

Building morphology  
Microclimate  
Deep Learning  
Building group  
Sun path  
Transfer learning

## ABSTRACT

Climate conditions play a pivotal role in estimating buildings' energy consumption. For urban-scale building energy dynamic simulation, the typical meteorological year weather represents a universal climate condition for the entire city. However, the varying terrain roughness, environment conditions, human-built architectures jointly formulate a unique microclimate condition for each building. This study intends to develop flexible and reliable approach to assess a building's microclimate condition based on its surrounding environment morphological features. The proposed approach leverages deep transfer learning neural networks that combines seasonal sun path trajectories and front projection maps of building groups. To validate the proposed method, a case study was conducted on a campus environment with wireless environmental sensing systems. The findings of this study demonstrate that the projection matrices and sun path can improve the assessment methods solely based on the dynamic impacts of urban morphological features and can forecast microclimate dynamics for urban-scale building energy simulation.

## 1. Introduction

With the continuous improvement of the social economy, the building sector is the principal consumer of urban energy usage, consuming approximately 30 % of the global energy consumption and concurrently serving as the major contributor to the worldwide carbon dioxide (CO<sub>2</sub>) emission [1,2]. The rapid population increase in recent years invariably augments the energy requisites of cities [3] due to the diverse needs of burgeoning citizens and the increasing demands of commercial development [4,5]. Hence, promoting building energy efficiency under the urban context is crucial in near future. The reliable and flexible evaluation of building energy performance emerges as a pivotal role in facilitating the meticulous optimization of energy usage and management of renewable energies [6].

Tools for building energy simulation (BES), such as EnergyPlus, have been extensively adopted to predict building energy demands and assess diverse energy-efficient designs. Unrealistic weather conditions can lead to substantial discrepancies between simulation results and the actual energy performance of buildings [7]. Most BES tools utilize weather files based on the Typical Meteorological Year (TMY), which are generated from weather station data spanning multiple years, typically collected at

wild. These universal weather files at a city scale assume uniform weather conditions for all buildings within the city. However, the actual urban environment is considerably more intricate than the suburban setting at an airport. For example, diverse building and vegetation characteristics give rise to intra-urban microclimate variations, such as the urban heat island (UHI) effect on the cooling demand, which can exhibit magnitudes comparable to differences between urban and suburban climates [8,9]. In a study analyzing a decade of hourly meteorological data from 27 local stations in San Francisco, Hong et al. documented pronounced fluctuations in urban microclimates and notable disparities in buildings' energy requirements [10]. Given that TMY files fail to accurately represent microclimate conditions in urban settings, multiple research studies have proposed integrating field-measured microclimate data obtained through localized sensors into BES for urban areas. By comparing BES outcomes with actual energy consumption patterns using various weather data inputs, Xu et al. demonstrated that microclimate data collected near the target buildings outperformed TMY data [11].

Within the urban context, microclimate emerges from intricate interplays between human activities, human-made structures, and the natural environment [12]. As a predominant urban element, buildings

\* Corresponding author.

E-mail addresses: [qili84-c@my.cityu.edu.hk](mailto:qili84-c@my.cityu.edu.hk) (Q. Li), [weiwang@seu.edu.cn](mailto:weiwang@seu.edu.cn) (W. Wang), [jiayuchen@tsinghua.edu.cn](mailto:jiayuchen@tsinghua.edu.cn) (J. Chen).

wield a more substantial climatic influence compared to greenery, for example the impact of the UHI effect [13]. Numerous researchers have substantiated that morphological attributes primarily drive buildings' impact on the local surroundings. One of the chief factors behind this influence is the shading effect, whereby buildings modify solar radiation [14,15]. However, prior investigations have predominantly concentrated on quantifying relationships between fixed morphological factors and microclimate conditions, overlooking the dynamic interplay between buildings and the evolving trajectory of the sun throughout the day [16–18]. Hence, to accurately capture microclimate data, it is pivotal to incorporate the influence of buildings' morphological features on natural environmental conditions like the sun's path. Given that building façades oriented toward the sun possess significant shading effects, this study seeks to extract morphological factors by correlating these façades with data streamed by various sensors. Given the impracticality and cost of deploying sensors citywide, there arises a need to develop dependable quantitative methodologies for assessing microclimate conditions at unsensed locations. To address both research gaps, this study endeavors to devise a deep learning approach for evaluating urban microclimate conditions using limited sensor inputs and the ever-changing building morphology induced by the sun's seasonal trajectory. To this end, this study proposed to approximate local microclimate conditions by calibrating TMY weather data with a transfer learning network that gauges microclimate conditions using local morphological attributes. The proposed method can quickly generate the local microclimate conditions based on the morphological conditions that surround a target location.

## 2. Background

### 2.1. Shading effects of buildings on urban microclimate

Microclimate typically refers to localized climatic patterns within a horizontal range of approximately 1 km, encompassing essential variables such as temperature, wind speed, humidity, and solar radiation [19,20]. Such urban climate conditions also can be affected by human interventions in the process of rapid social and economic development [21,22]. The design of the built environment can profoundly alter urban microclimate conditions [23]. A notable instance is the discernibly lower physiological equivalent temperature observed in shaded areas compared to unshaded spaces, with differences reaching up to 27 °C [24]. Previous studies have emphasized the pivotal role of buildings' shading effects in shaping heterogeneous urban microclimates. This effect arises from the obstruction of solar irradiation and reduction of heat accumulation within urban landscapes [25]. Also, the movement of the sun along its path can change the shading surfaces of buildings, resulting in various shadow sizes and locations [26]. When shadows fall on a building's surface or land, the received solar radiation within a target area is reduced, leading to variations in local thermal conditions that can further influence other micro-climate patterns such as relative humidity [18]. Additionally, the surface reflectivity of land and buildings differs, meaning that even areas receiving the same amount of light can result in different solar energy gains within a local area [24]. Substantial efforts have been devoted to aligning building orientation and the angle of solar incidence to ameliorate extreme thermal conditions in urban locales. Several investigations suggest that a north-south street orientation can optimize outdoor thermal conditions by maximizing building shading benefits [27].

Beyond building orientation, the geometry and layout of structures also wield fundamental influence on solar access. Wai et al. formulated a computational fluid dynamics (CFD) model to assess the shading impacts of diverse building forms, pinpointing the reduction of building lengths as the most effective approach to mitigate solar irradiance reaching the ground in urban settings [28]. Perini and Magliocco employed the ENVI-met microclimate simulation to scrutinize how buildings influence the urban thermal environment. Their findings

underscored that the average height and density of buildings substantially affect potential temperature and mean radiant temperature due to shading effects [29]. While CFD software (such as ENVI-met, Fluent, CitySim) can unveil the physical dynamics of building shading on microclimate, the modeling process often involves simplification due to demanding computational requirements [30]. Sharmin et al. revealed limitations in the CFD approach, particularly in reproducing air temperature variations attributed to different building geometries [31]. To surmount CFD's limited morphological sensitivity, researchers advocate for the development of quantitative building morphological factors to characterize the climatic implications of building shading [32–34]. For instance, the sky view factor (SVF), representing sky visibility, exhibits a positive correlation with daytime temperature [35]. The aspect ratio (H/W), indicating the ratio of average building height to street width, holds a substantial relationship with the urban thermal environment by influencing heat dispersion [36]. Nonetheless, only a few morphological factors have been explored, and their quantitative connection to the shading impact of buildings remains unclear. This underscores the considerable potential for devising more effective building morphological parameters to accurately quantify buildings' shading effects and estimate urban microclimate conditions.

### 2.2. Quantitative morphological features of buildings

The arrangement and geometries of buildings stand as pivotal driving forces in shaping microclimate conditions within urban areas [3]. In the early stages, researchers primarily concentrated on depicting land cover patterns through two-dimensional (2D) horizontal building morphologies [37]. These factors, such as percent landscape (PLAND) and patch density (PD), are derived from building footprints and can effectively elucidate the spatial variations in urban thermal conditions [38]. The explicit connection between 2D building morphological factors and urban microclimate conditions allows for straightforward quantification through linear regression [39]. Beyond the realm of 2D horizontal characteristics, buildings possess a distinctive vertical composition, prompting an expansion to incorporate three-dimensional (3D) morphological features. 3D building morphological factors encompass measurements of building height, volume, sky view factor (SVF), as well as distinctive attributes like floor area ratio (FAR) [17,40]. In a study by Yu et al., a comparison of the impact of 2D and 3D building morphological factors on land surface temperature revealed the superior capacity of 3D factors to accurately quantify the undulations and complexities of land patterns and thereby expound on variations in the urban thermal environment compared to 2D factors [41]. Similarly, Tian et al. reported that 3D morphological characteristics more effectively accounted for air temperature variations, with building height emerging as the most significant nocturnal indicator [42]. Among these 3D morphological factors, the frontal area index (FAI) takes precedence due to its relevance in urban ventilation and its primary applicability in assessing the UHI effect [43]. An advantage of FAI lies in its capacity to delineate buildings' height and width across various wind directions, thus mitigating the loss of spatial information when compared to other 2D or 3D morphological factors [44]. Moreover, assessing the frontal area across different height levels allows for a more accurate portrayal of urban surface roughness [45]. Shi et al. divided building frontal areas into three height tiers (0–15 m, 15–60 m, and 60 m above), demonstrating that these divided FAIs exhibit a stronger correlation with the dispersion of urban air pollution than the total FAI [46]. Building upon this, Li et al. developed three distinct approaches for segmenting frontal area stripes in both horizontal and vertical directions, highlighting the value of meticulous frontal area division in assessing urban microclimate conditions [47]. In summary, a multitude of researchers have underscored the quantifiable impact of both 2D and 3D building morphological factors on microclimate conditions, emphasizing that furnishing a more intricate depiction of building geometry serves as a pivotal focal point in microclimate assessment.

### 2.3. Data-driven methods for microclimate assessment

To address the limitations inherent in standard weather data for urban building energy modeling, there is a growing trend towards the adoption of data-driven methodologies such as deep learning neural networks. With various sensors, environment information heat, light, chemistry and biology [48] can be processed with sensor data analytics and artificial intelligence algorithms [49]. Unlike time-consuming physical simulations, these methods utilize historical time-series data to establish site-specific microclimate assessments [50,51]. Leveraging artificial neural networks (ANN), Kolokotroni et al. successfully formulated an hourly air temperature prediction model for London, demonstrating acceptable temporal and spatial validity [52]. Ghimire et al. undertook the development and evaluation of various machine learning approaches for forecasting global solar radiation, with ANN emerging as the superior method over Gaussian process machine learning (GPML), support vector regression (SVR), and genetic programming (GP) models [53]. While these conventional ML techniques adeptly capture the non-linear nature of weather data, their performance in time-series applications is constrained by their short-term memory foundation [54]. Diverging from standard feed-forward neural networks, recurrent neural networks (RNNs) like long-short term memory networks (LSTM) are better suited for processing time-series data due to their memory state capability. Zhang et al. successfully employed LSTM models to achieve high accuracy in predicting one-day-ahead temperature, relative humidity, and solar radiation values [7]. In pursuit of heightened microclimate prediction accuracy, Han et al. integrated locally-measured sensor data with extensive historical weather records from an airport to develop a localized weather prediction model. This integration significantly improved the accuracy of the RNN model through knowledge transfer [55]. Similarly, Ma et al. effectively predicted air quality at a new station by transferring data from an existing station with comparable geographical conditions [56]. In addition to directly transferring pertinent knowledge, Li et al. highlighted the substantial enhancement achievable in microclimate prediction models by incorporating transferred building morphological information specific to the target location [47]. Nonetheless, their study failed to consider the interplay between building morphologies and natural environmental factors like wind direction and sun path, which indirectly contribute to microclimate variations. Consequently, there exists a potential to refine microclimate assessments through knowledge transfer mechanisms that more comprehensively reflect microclimate formation dynamics. Based on the findings of these studies, this research aims to develop a deep learning model that transfers morphological attributes obtained from buildings' frontal areas based on solar paths. A modified LSTM model is devised to predict microclimate conditions at various locations using on-site sensor data. The transferred knowledge comprises a range of traditional 2D and 3D building morphological factors along with graph-like frontal area data. By employing two projection techniques, a binary 2D matrix is generated to represent the frontal areas of buildings that face the sun's trajectory.

## 3. Methodology

### 3.1. Sun-path-dependent morphological deep transfer learning neural networks

The shading effect exerted by the neighboring buildings emerges as a determinant in reshaping climatic conditions within urban areas. Drawing inspiration from this observation, this study intends to introduce a dual-branch deep transfer learning neural network aimed at refining microclimate prediction through the interplay between sun path and building morphologies. The first branch encompasses a selection of conventional quantitative 2D and 3D morphological factors, widely employed in the evaluation of urban environments. The second branch incorporates binary 2D matrices of buildings' frontal areas,

computed using two distinct projection methods. These features are derived by identifying the pertinent slice based on the dynamic sun's path. To generate the frontal area matrices, this study introduces two novel projection methods: parallel projection gridding and surrounding projection gridding. In detail, the parallel projection gridding will use a vertical plane that is perpendicular to standard directions (North, Northeast, East, etc.) to obtain the gridding data of the building group, while the surrounding projection will adopt a cylindrical surface that encircles the target area to generate gridding data. The basic ontology of the proposed networks is shown in Fig. 1.

Fig. 1 depicts the framework of the proposed sun-path-dependent morphological deep transfer learning neural networks. The input data for the model comprises time-series microclimate data gleaned from sensor readings, encompassing essential urban environmental parameters measured onsite at high resolution for the designated location. These parameters encompass air temperature, relative humidity, carbon dioxide (CO<sub>2</sub>) concentration, total volatile organic compound (TVOC) concentration, and illumination intensity.

The building geometry-related inputs include static, conventional 2D and 3D morphological factors, alongside graph-like frontal area data contingent on the sun path. The climate-related inputs are processed through LSTM and fully connected layers to yield a first-order prediction of hourly climate conditions. In tandem, the building geometry-related inputs entail further decomposition of the 2D matrices representing frontal areas. This decomposition involves the selection of the specific slice that directly faces the sun based on the solar azimuth angle. The sun path for a specific geo-location is stable over the years. This study utilized the solar azimuth angle data to reflect the seasonal variation of the sun path. The solar azimuth angle usually has an hourly data resolution in most weather files. Subsequently, this chosen slice undergoes processing through a Convolutional Neural Networks (CNN) module to extract distinctive features. Following this, the extracted features, derived from both the 11 conventional factors and the frontal area, are input into fully connected layers alongside the initial climate condition prediction outcomes. The integration of tuning residuals and first-order predictions culminates in the computation of the ultimate microclimate condition results for the designated area. The inputs of data tuning starts from the city's TMY weather file. The TMY file is usually provided by the local meteorological department based on long-term climate observations with local weather stations. In general, the TMY file was created based on averaged climate conditions over 10 years and provides detailed daily weather conditions for a whole year.

### 3.2. 2D/3D morphological attributes and the frontal area matrixes

Within this study, the initial category of building geometry-related inputs comprises the conventional 2D/3D morphological factors, which elucidate the static spatial arrangement and configuration of structures within the designated area. The second category encompasses the frontal area matrices of building envelopes, interconnected with the sun's path. A comprehensive compilation of all the 2D/3D morphological factors employed in this study is presented in Table 1. Buildings situated within a 50-m radius are chosen to calculate the complete set of 11 morphological factors, as detailed in the calculation equations outlined in Table 1. Among the 2D morphological factors, the inclusion consists of patch area range (PAR), percentage of patch (PLAND), coefficient of variation (CV), largest patch index (LPI), and patch density (PD). As for the 3D morphological factors, this study encompasses building volume density (BVD), building height range (BHR), building height density (BHD), building otherness (BO), highest building index (HBI), and building surface area (BSA).

The frontal area index ( $\lambda_f$ ) is essential in appraising the inherent roughness of urban terrain and assessing the ventilation potential within urban environments. It is computed by dividing the total area of all building facets projected onto the plane normal to the specific wind direction ( $A_f$ ) by the planar area of the designated location ( $A_T$ ), as

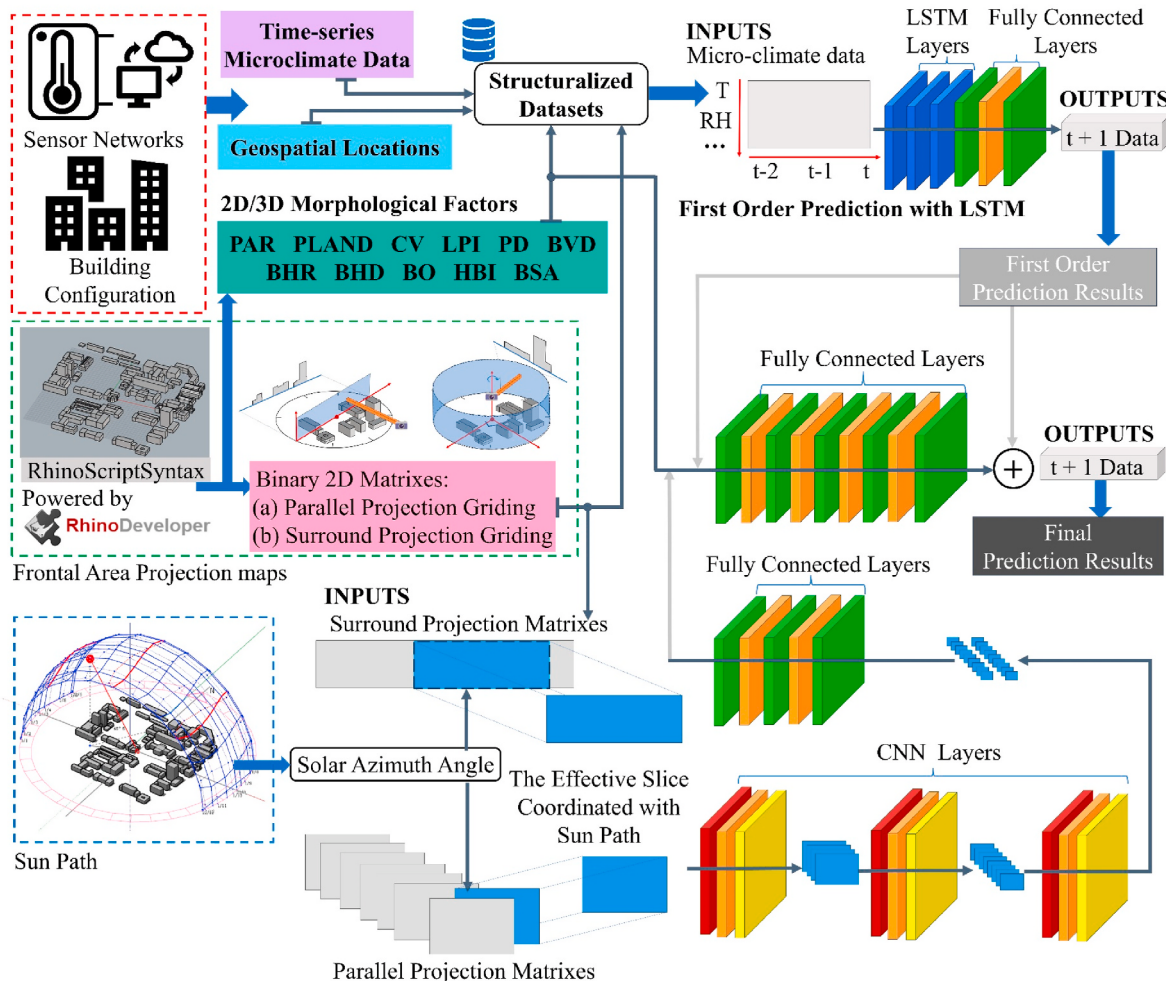


**Fig. 1.** The framework of the proposed sun-path-dependent morphological deep transfer learning neural networks.

depicted in Equation (1) [43].

$$\lambda_f = A_F / A_T \quad (1)$$

The process of calculating binary 2D frontal area matrices is depicted in Fig. 2, where two projection techniques are devised to break down the frontal area (greyscale colors indicate the depth of 3D projection on the projection surface). As illustrated in Fig. 2(a), the parallel projection gridding involves creating a projection surface (depicted in light blue) that stands perpendicular to the projection direction. This surface passes through the central point of the target area to capture the shadows of buildings cast by an array of parallel light sources along the height and width dimensions. Each target location generates projection maps in eight directions (north, south, east, west, northeast, northwest, southeast, and southwest). The map with the minimum angle between the solar azimuth and the projection direction is selected as the effective slice for matrix generation. In the context of the surrounding projection gridding, illustrated in Fig. 2(b), the projection surface is a cylindrical facade (depicted in light blue) formed around the central point of the target area. The light source is positioned at the central axis of the cylinder. A succession of lights project perpendicularly onto the surface along both the height and azimuth angle dimensions. The projection map resulting from the surround projection gridding is a 2D rectangular surface achieved by unfolding the cylindrical facade. The effective slice of the map is a half facade within a  $\pm 90^\circ$  range of the solar azimuth angle. To streamline the process, projection maps obtained through both methods are then converted into binary 2D matrices. As depicted in Fig. 2(c)—a 2D grid is employed to divide each projection map vertically

and horizontally. In line with an illustrative study, a 2-m interval is utilized for the grid cutting. Each grid point generates a binary value (BV), ultimately yielding a final data structure in the form of a 2D matrix  $[X, Y]$  as described in Equation (2). Here, X signifies the number of rows, and Y signifies the number of columns.

$$[X, Y] = \begin{bmatrix} BV_{11} & \dots & BV_{1Y} \\ \vdots & \ddots & \vdots \\ BV_{X1} & \dots & BV_{XY} \end{bmatrix} \quad (2)$$

The detail of the binary value (BV) calculation is shown in Equation (3):

$$BV = \begin{cases} 1 & \text{if : } \int_{x_1}^{x_2} \int_{y_1}^{y_2} f(x, y) d_x d_y > 0 \\ 0 & \text{Other} \end{cases} \quad (3)$$

Where  $x_1$  and  $x_2$  are horizontal coordinate values of the left bottom and the right top of a grid ( $G_1, G_2, G_3 \dots$ );  $y_1$  and  $y_2$  are vertical coordinate values of a grid's left bottom and right top ( $G_1, G_2, G_3 \dots$ );  $f(x, y)$  is the area distribution function of buildings.

### 3.3. Hybrid deep transfer learning module

The hybrid deep transfer learning module proposed in this study encompasses two principal branches designed to manage climate-related and building-geometry-related inputs. Within this module, LSTM layers serve as the core component of the primary data processing branch, resulting in comparatively accurate microclimate predictions

**Table 1**

List of the building morphology attributes.

Metrics	Equation	Description	Reference
Patch area range (PAR)	$a_{max} - a_{min}$	where $a_{max}$ is the area of the largest building patch and $a_{min}$ the area of the smallest building patch	[18]
Percentage of patch (PLAN)	$\frac{\sum_{i=1}^n a_i}{A} \times 100\%$	where $a_i$ is the area of building patch $i$ and $A$ the buffer area	[18]
Coefficient of variation (CV)	$\sqrt{\frac{1}{n} \sum_{i=1}^n (a_i - \bar{a})^2}{\bar{a}}$	where $a_i$ is the area of building patch $i$ and $\bar{a}$ the average area of building patches	[57]
Largest patch index (LPI)	$\frac{\sum_{i=1}^n \max(a_i)}{A} \times 100\%$	where $\max(a_i)$ is the area of the largest building patch and $A$ the buffer area	[37]
Patch density (PD)	$\frac{n}{A}$	where $n$ is the number of building patches and $A$ is the buffer area	[37]
Building volume density (BVD)	$\frac{\sum_{i=1}^n V_i}{A}$	where $V_i$ is the volume of building $i$ (volume = footprint $\times$ height) and $A$ the buffer area	[58]
Building height range (BHR)	$H_{max} - H_{min}$	where $H_{max}$ is the height of the tallest building and $H_{min}$ the height of the lowest building	[57]
Building height density (BHD)	$\frac{\sum_{i=1}^n H_i}{A} \times 100\%$	where $H_i$ is the height of building $i$ and $A$ the buffer area	[12]
Building otherness (BO)	$\sqrt{\frac{1}{n} \sum_{i=1}^n (H_i - \bar{H})^2}{\bar{H}}$	where $H_i$ is the height of building $i$ and $\bar{H}$ the average height of buildings	[57]
Highest building index (HBI)	$\frac{\sum_{i=1}^n \max(H_i)}{\sum_{i=1}^n H_i} \times 100\%$	where $\max(H_i)$ is the height of the tallest building and $H_i$ the height of the building $i$	[57]
Building surface area (BSA)	$\sum_{i=1}^n S_i$	Where $S_i$ is the area of one surface of a building	[59]

grounded in time-series sensor data. Notably, LSTM incorporates a memory cell, denoted as  $C_t$ , which functions to store and transmit preceding information forward. The memory cell's state,  $C_t$ , is regulated by three gates: the input gate,  $i_t$ , the output gate,  $o_t$ , and the forget gate,  $f_t$ . These gates collectively facilitate the selective retention of long-term temporal data. The mathematical formulation of LSTM is presented as follows:

$$x_t = [x_{t1} \ x_{t2} \ x_{t3} \dots x_m] \quad (4)$$

$$i_t = \text{sigmoid}(W_i \bullet [h_{t-1}, x_t] + b_i) \quad (5)$$

$$o_t = \text{sigmoid}(W_o \bullet [h_{t-1}, x_t] + b_o) \quad (6)$$

$$f_t = \text{sigmoid}(W_f \bullet [h_{t-1}, x_t] + b_f) \quad (7)$$

$$C_t = f_t * C_{t-1} + i_t * \tanh(W_c \bullet [h_{t-1}, x_t] + b_c) \quad (8)$$

$$h_t = o_t * \tanh(C_t) \quad (9)$$

Where  $x_t$  represents the input vector of the LSTM unit and  $x_{tn}$  represents the  $n$ -th micro-climate parameter at time  $t$ ;  $h_t$  is the output of the current LSTM unit at time  $t$ ;  $\tanh$  and  $\text{sigmoid}$  are the activation functions;  $W_i$ ,  $W_o$ ,  $W_f$  and  $W_c$  are weight matrixes;  $b_i$ ,  $b_o$ ,  $b_f$  and  $b_c$  are the bias vectors.

Fig. 3 illustrates the network structure of the conventional LSTM model, solely utilizing time-series sensor readings as inputs. In contrast, the building morphological transfer learning model (LSTM-M) extends to incorporate five fully connected layers (FC layers) that serve as the transfer learning component. This model integrates two distinct input branches. The first encompasses the first-order prediction results ( $x_F$ )

generated by three LSTM layers and two FC layers, while the second involves the incorporation of eleven 2D/3D morphological factors. To streamline the input feeding process for the transfer learning component, these two input branches are initially merged to generate the actual input vector,  $x_A$ , as depicted in Equation (10):

$$x_F = [x_A \ x_{M1} \ x_{M2} \ x_{M3} \dots \ x_{Mn}] \quad (10)$$

Where  $x_{Mn}$  is the  $n$ -th 2D/3D morphological factors.

The LSTM-M model exhibits notable distinctions in terms of data characteristics and layer structures between the conventional LSTM block (comprising 3 LSTM layers with 2 FC layers) and the transfer learning component block (comprising 5 FC layers). Directly concatenating these two blocks could readily lead to model degradation, a prevalent concern during the optimization process. Hence, in lieu of directly generating prediction outcomes from the five FC layers, a residual mapping strategy is adopted to enhance the model training procedure. This layer structure design aligns with the principles underpinning the concept of deep residual networks (ResNet) [60]. ResNet deviates from the approach of having stacked layers solely match a desired underlying mapping  $H(x)$ . Instead, it employs a residual mapping  $F(x) := H(x) - x$  as a substitute for the fitting process, effectively reformulating the initial mapping as  $F(x) + x$ . This modification significantly streamlines the optimization of the residual mapping [60]. In our model, the incorporation of a residual mapping design ensures that the ultimate prediction results from the model, incorporating morphological inputs, will invariably equal or surpass the first-order prediction results stemming solely from climate inputs.

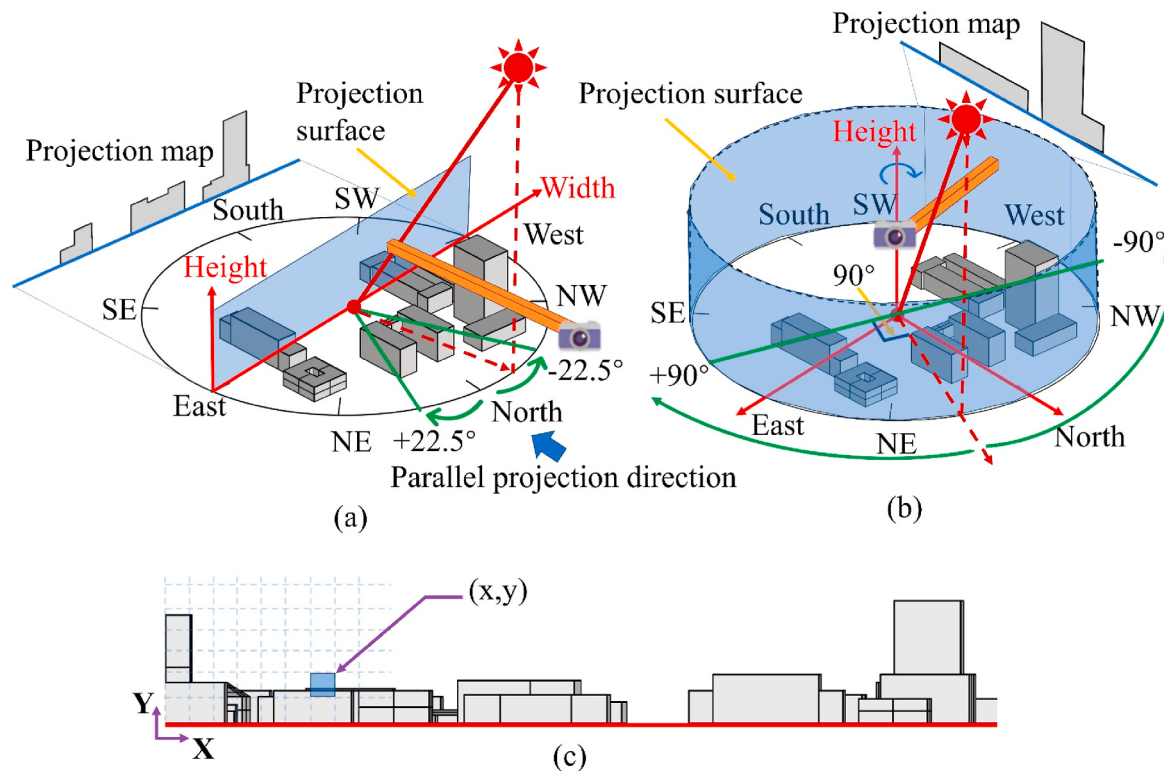
The Sun-path-dependent Morphological Deep Transfer Learning model with parallel projection matrix (SP-P) and the Sun-path-dependent Morphological Deep Transfer Learning model with surrounding projection matrix (SP-S) expand upon the LSTM-M model's framework by incorporating embedded CNN structures to process graph-like binary 2D matrices. Illustrated in Fig. 4, the parallel projection matrices encompass eight binary 2D matrices, each generated from distinct directions: north, south, west, east, northwest, northeast, southwest, and southeast. The selection of the pertinent slice hinges on the proximity between the projection direction of the 2D matrix and the solar azimuth angle at the specific time of microclimate prediction. For instance, let's consider the scenario where the solar azimuth angle at  $t+1$  falls within a range of  $\pm 22.5^\circ$  of a particular projection direction, such as north. In this instance, the 2D matrix projected in the north direction is selected and input into the CNN structures. In comparison, the surround projection matrix boasts a more adaptable data structure that harmonizes projection direction with the sun's path. Depicted in Fig. 5, projection data within a  $\pm 90^\circ$  range of the solar azimuth angle at  $t+1$  is designated as the effective slice.

Table 2 summarizes the structure of all network models. The proposed deep transfer learning neural network has three Conv2d layers extends three pooling layers form the CNN structure. The activation function is rectified linear unit (Relu); trial epochs is 100; the learning rate of the first 50 epochs is 0.0001 and 0.00001 for the last 50 epochs. The loss function is the mean squared error loss function (MSELoss) with the Adaptive Movement Estimation algorithm (Adam) as optimizer.

## 4. Validating study

### 4.1. Experiment sites and micro-climate data collection

To assess the efficacy of the proposed methodology, this study conducted validation experiments within the Sipailou campus of Southeast University, situated in Nanjing, Jiangsu Province, China (Longitude: 118.80 E, Latitude: 32.06 N). The experiment site falls within the humid subtropical monsoon climate zone, characterized by temperate conditions and four distinct seasons. Local precipitation is abundant, with an annual average of 1106 mm. The yearly mean temperature stands at



**Fig. 2.** Frontal area matrixes generation method: (a) parallel projection gridding, (b) surrounding projection gridding, and (c) generation of binary 2D frontal area matrix.

15.4 °C, with the highest extreme reaching 39.7 °C and the lowest at -13.1 °C. For the city morphology, Nanjing has a high building density index with a mean value of 1.93 and an extensive average building height index of 13.4 [57]. Additionally, the vegetation is relatively low, with mean forest index values of 2.73 [57]. For detailed insight into Nanjing's climate conditions, reference can be made to the China Meteorological Data Service Centre (<http://data.cma.cn>). The validation experiment was conducted between November 30th, 2020 and December 31st, 2020. Sixteen portable measurement sites were strategically selected across the experimental site, each representing varied built environments, as showcased in Fig. 6.

The validation experiment utilized integrated sensor modules made of capacitive-resistive devices attached to a control board. At each site, a wireless sensor node was affixed at approximately 1.2 m above ground level on a pole, measuring five environmental parameters: temperature, relative humidity, illumination intensity, carbon dioxide (CO<sub>2</sub>) concentration, and total volatile organic compound (TVOC) concentration. These collected data were stored locally and transmitted to the cloud via Wi-Fi channels at 5-min intervals. Basic information about the sensors is summarized in Table 3. Since the temperature and relative humidity data served as the baseline for deep learning training, this study conducted a validation test of the sensors by comparing the results with an on-campus microclimate station. The sensor was installed near the microclimate station mounted on poles at a height of 1.2 m and collected 24-h data. The microclimate station was from the Onset Computer Corporation ([www.onsetcomp.com](http://www.onsetcomp.com)). The details of the microclimate station are shown in Table 4. The test results proved that the temperature sensor has an accuracy of ±0.5 °C and the relative humidity is ±2 %.

#### 4.2. Data preprocessing and preparation of climatic dataset

There are some missing data due to uncontrolled reasons, such as instrument malfunctions. In the study, the sensor's battery life is three

days. The batteries of all 16 sensors are replaced periodically within three days. Data loss is unavoidable due to various reasons. Therefore, when a data section is invalid or missing for more than 1 h, that sensor node is considered invalid for processing during that period. During the data preprocessing stage, if a sensor's failure duration surpasses 1 h, the corresponding missing data is deemed invalid and subsequently removed from the raw dataset. Conversely, instances of missing data with a duration less than 1 h are addressed through linear interpolation. The raw data related to the five environmental parameters is transformed using a 3-h sliding window to generate the 3-h historical climate data, which is then used to forecast microclimate conditions. Subsequently, the output dataset is divided into 1-h segments. In the LSTM unit, consecutive time-series data at  $t$ ,  $t-1$ , and  $t-2$  are inputted, ultimately generating the output for  $t+1$ . Essentially, the developed models are designed to utilize the climate data from the previous 3-h records to forecast microclimate conditions for the subsequent hour. The training and testing sets are constructed from the comprehensive dataset, wherein 80 % of the data (8859 samples) constitutes the training set, and the remaining 20 % (2224 samples) comprises the testing set.

#### 4.3. Buildings' morphological inputs

In this study, the microclimate assessment zone for each measurement site was delineated by a circular area with a radius of 50 m, centered at the sensor installation location. The computation of 2D/3D building morphological factors was executed in accordance with the equations detailed in Table 1. To streamline the projection process, a series of  $2 \times 2 \times 50$  blocks were designed. If a block intersected with buildings within a zone, the matrix element would be assigned a value of '1'; otherwise, the element value would remain '0'. Given that the maximum building height on campus is below 60 m, the height range for both projection methods was set at 60 m. The interval for height and width increments was defined as 2 m in both projection processes.

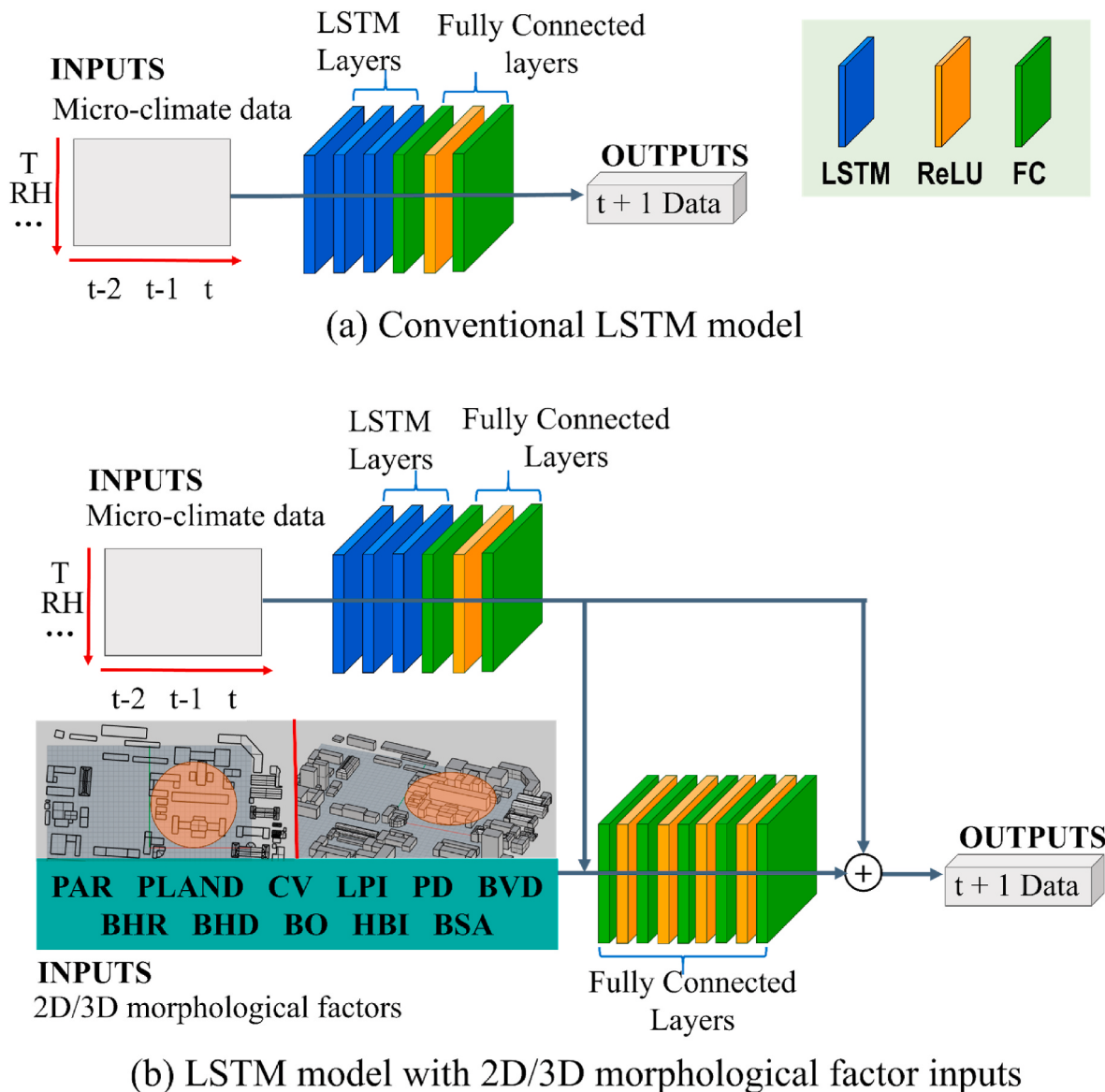


**Fig. 3.** The conventional LSTM model and the LSTM-M model.

In the case of parallel projection, the width corresponds to the diameter of a zone (100 m). The ultimate data structure resulting from parallel projection within each zone is an 8 by 30 by 50 matrix, encompassing 8 directions, 30 rows, and 50 columns. Conversely, due to the cylindrical nature of surround projection, the width increment interval is translated into an angular degree. To achieve a 2-m grid interval, an angle of  $\pi/75$  is set in a clockwise direction. This computation yields a 30 by 150 matrix for each zone via surround projection.

#### 4.4. Model construction and error measurement metrics

All four models shown in Table 2 were programmed with PyTorch. The computational setup employed during the validation experiment was a PC equipped with the Windows 11 OS, powered by an Intel(R) Core i5 8300H CPU, 8 + 16 GB DDR4 RAM, and an Nvidia GTX 1060 GPU. Evaluation of the prediction errors for the four models was conducted using two metrics: the root mean squared error (RMSE) and the mean absolute error (MAE). The over-prediction ratio (OPR) is equal to the number of prediction values larger than the baseline divided by the total number of prediction values. To offer a more comprehensive representation of the precision in predicting microclimate conditions,

temperature prediction accuracy was defined within three ranges:  $\pm 1^{\circ}\text{C}$ ,  $\pm 2^{\circ}\text{C}$ , and  $\pm 3^{\circ}\text{C}$ . These ranges signify that the absolute difference between the predicted value and the actual value falls within  $1^{\circ}\text{C}$ ,  $2^{\circ}\text{C}$ , or  $3^{\circ}\text{C}$ , respectively. Similarly, the assessment of relative humidity accuracy entailed  $\pm 5\%$ ,  $\pm 10\%$ , and  $\pm 15\%$  ranges. All these metrics for model evaluation are summarized in Table 5.

## 5. Results

### 5.1. Prediction results of temperature

The training errors of the four deep learning models for temperature prediction are presented in Fig. 7. When juxtaposed with the LSTM model, the models incorporating building-geometry-related inputs exhibit an enhancement in RMSE. Moreover, the inclusion of transferred morphological features aids in hastening error convergence and heightening the efficiency of the training process. The testing dataset's prediction accuracy within the ranges of  $\pm 1^{\circ}\text{C}$ ,  $\pm 2^{\circ}\text{C}$ , and  $\pm 3^{\circ}\text{C}$ , as well as the corresponding RMSE and MAE, are comprehensively summarized in Table 6.

EnergyPlus weather file (EPW) has the lowest accuracy and under

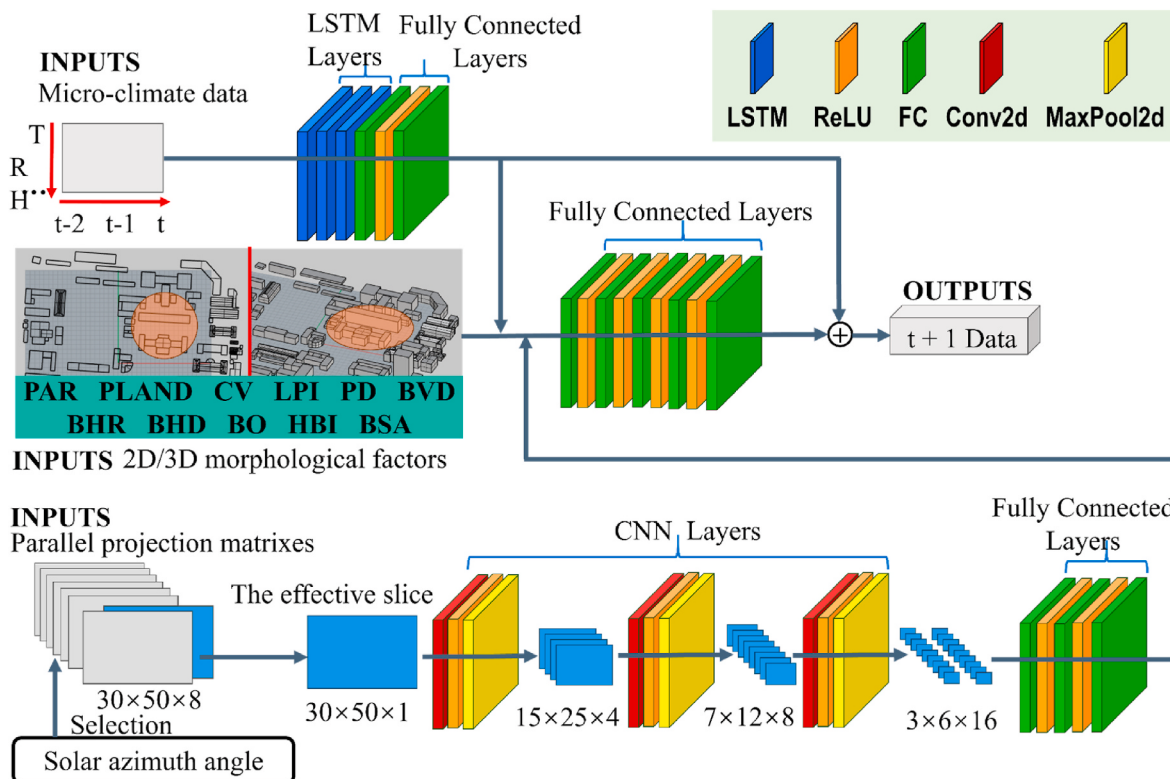


Fig. 4. Network structure of the SP-P model.

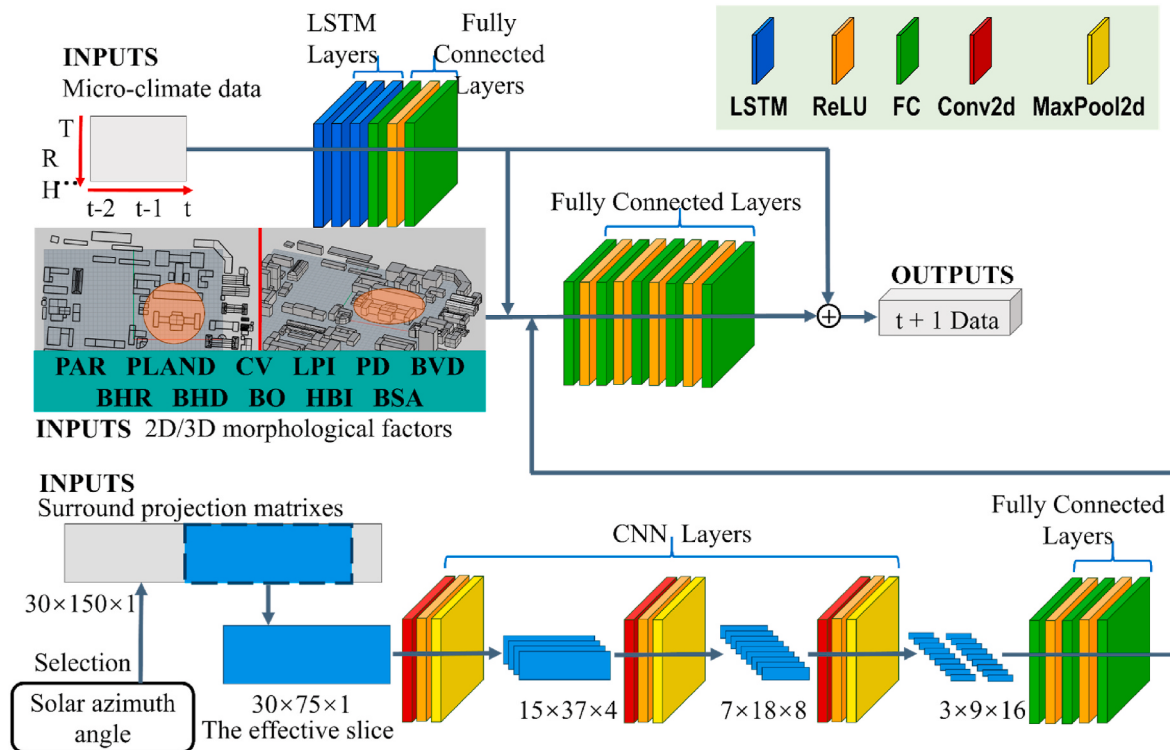


Fig. 5. Network structure of the SP-S model.

estimated the local temperature. In an overall assessment, the inclusion of morphological features proves instrumental in augmenting prediction accuracy and mitigating prediction errors. Since the OPR of four deep learning models is larger than 50 %, they over predict the local

temperature. Notably, the LSTM-M model incorporating 11 static morphological factors yields a modest enhancement in temperature prediction. When juxtaposed with the LSTM model, the LSTM-M model achieves a marginal 3.8 % increase in accuracy within 1 °C, a 3.3 %

**Table 2**  
List of transfer learning neural networks.

Model name	List of Input	Structures
Conventional LSTM model (LSTM)	- Time-series data from sensor reading.	-3 LSTM layers + 2 FC layers
LSTM model with morphological feature layers (LSTM-M)	- Time-series data from the sensor reading -11 morphological factors	-3 LSTM layers + 2 FC layers -5 FC layers
Sun-path-dependent transfer learning model with parallel projection matrix (SP-P)	- Time-series data from the sensor reading -11 morphological factors - 2D projection matrixes of the frontal area	-3 LSTM layers + 2 FC layers -5 FC layers -3 Conv2d layers + 3 MaxPool2d layers + 3 FC layers
Sun-path-dependent transfer learning model with surround projection matrix (SP-S)	- Time-series data from the sensor reading -11 morphological factors - 2D projection matrixes of the frontal area	-3 LSTM layers + 2 FC layers -5 FC layers -3 Conv2d layers + 3 MaxPool2d layers + 3 FC layers

improvement within 2 °C, and a 3.5 % advancement within 3 °C. Moreover, the RMSE and MAE values of the LSTM-M model register reductions of 13.7 % and 10.9 %, respectively. Conversely, the prediction efficacy of the SP-P and SP-S models demonstrates significant improvement over the LSTM model. Among them, the most robust prediction model, SP-P, yields noteworthy increments of 26.7 %, 19.6 %, and 17.3 % in accuracy within 1 °C, 2 °C, and 3 °C, respectively. Similarly, the RMSE is diminished by 42.2 %, while the MAE experiences a 44.3 % reduction. Hence, it is evident that sun path-dependent frontal area matrices wield greater effectiveness in predicting temperature variations.

**Table 3**  
Basic information for sensors (sampling rate is 5 min per-sample).

Environment Data	Sensor Model	Precision	Range	Resolution
Temperature	DHT22	±0.5 °C	-40 °C–80 °C	0.1 °C
Relative humidity	DHT22	±2 %	20 %-90 %	1 %
Illumination intensity	BH1750FVI	1lx	1lx to 65535 lx	1 lx
CO <sub>2</sub> concentration	CCS811	1 ppm	400 ppm–29206 ppm	1 ppm
TVOC concentration	CCS811	1 ppb	0 ppb to 32768 ppb	1 ppb

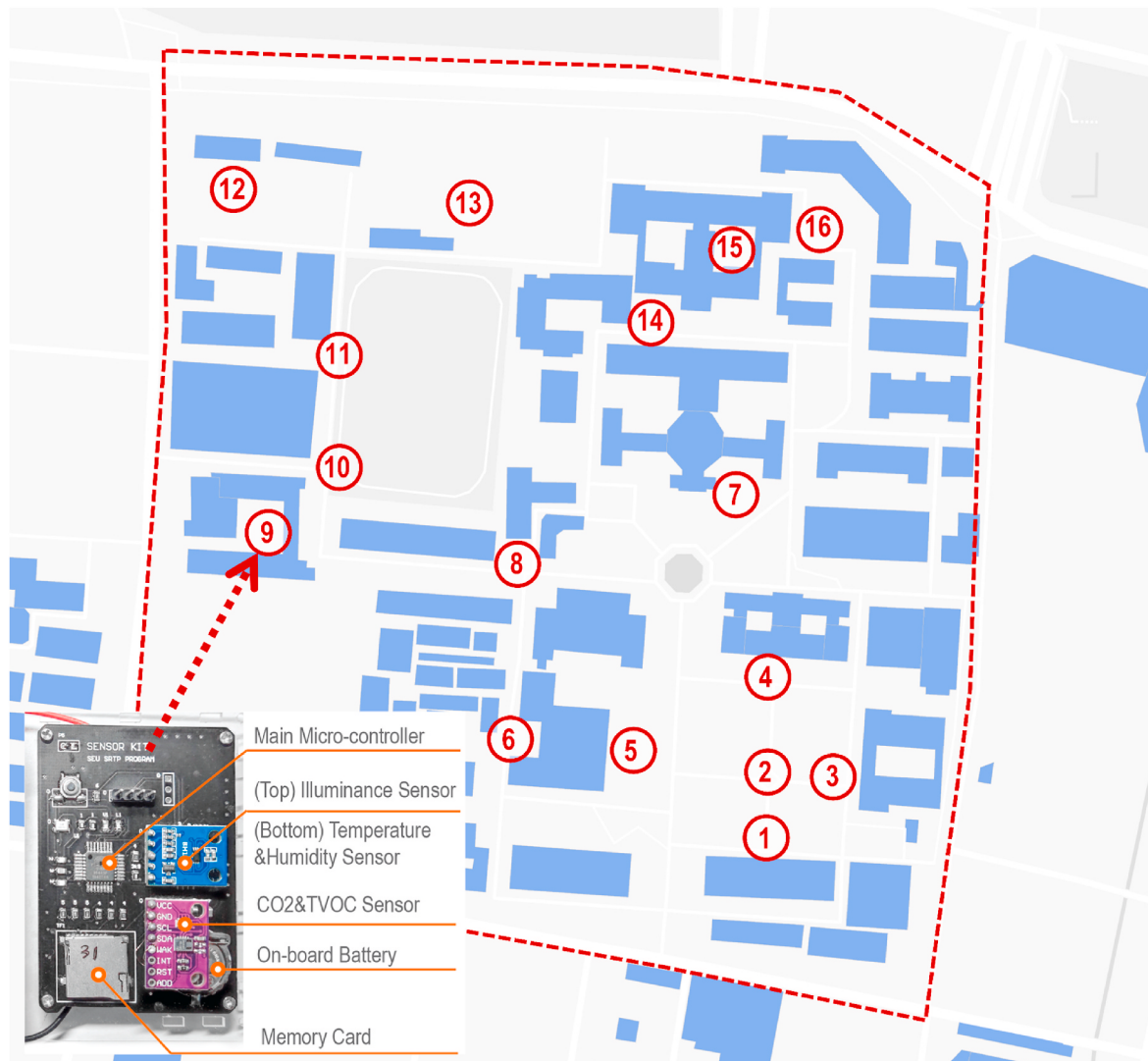


**Fig. 6.** Sensor nodes and install locations.

**Table 4**  
Basic information for sensors on the microclimate station.

	Data Logger	Temperature (T) /Relative Humidity (RH)	Wind Speed	Wind Direction	Solar Radiation
Version	RX3003	S-THB-M002	S-WSB-M003	S-WDB-M003	S-LIB-M003
Operating temperature	-40 to +60 °C	-40 to +75 °C	-40 to +75 °C	-40 to +70 °C	-40 to +75 °C
Accuracy	T: ±0.21 °C RH: ±2.5 %	±1.1 m/s or ±4 %	±5°	±10 W/m <sup>2</sup> or ±5 %	
Resolution	-	T: 0.02 °C RH: 0.1 %	0.5 m/s	1.4°	1.25 W/m <sup>2</sup>
Measurement range	-	T: -40 to +75 °C RH: 0–100 %	0–76 m/s	0–355°	0–1280 W/m <sup>2</sup>
Size (mm)	186(H) × 181(L) × 118(W)	10 × 35	410 × 16	460 × 200	41(H) × 32(Φ)

Fig. 8 illustrates the real-time temperature in comparison with the prediction outputs of the four models over the course of a typical day. The baseline curve is the measurement data from sensors. Notably, the LSTM-M model has the largest prediction error after sunset, during the periods of consistent nocturnal temperatures from 0:00 to 7:00 and 18:00 to 23:00. Within this period, the model performance of LSTM, SP-P, and SP-S is similar. This result indicates that static building morphologies have a low impact at night. After sunrise, all three deep learning models with morphological inputs demonstrate better performance than the LSTM model. Additionally, the temperature prediction results of SP-P and SP-S are closer to the baseline, except for the value of SP-S at 14:00. This observation underscores the significance of aligning building morphologies with the sun's path, as it significantly amplifies the accuracy of the model's temperature predictions.

To better demonstrate the significance of associating building morphologies with the sun's path, the performance of all models during the daytime (solar elevation angles larger than 0) was calculated and presented in Table 7. SP-P and SP-S, which incorporate environment-related morphological features, exhibit higher temperature prediction accuracy compared to LSTM and LSTM-M, with only slight over-prediction. This result indicates that calculating the frontal area matrix based on the changing sun angle can effectively enhance temperature prediction during the daytime.

## 5.2. Prediction results of relative humidity

Fig. 9 depicts the training errors of the four models for relative humidity prediction. Notably, the incorporation of morphological inputs proves to be a catalyst in hastening the convergence of RMSE values. In this context, the sun-path-dependent morphological features extracted from SP-P and SP-S models outperform the static factors of the LSTM-M model in terms of efficiency. Moreover, both SP-P and SP-S models attain a lower final training RMSE when contrasted with the LSTM and LSTM-M models.

The comprehensive prediction accuracy within ±5 %, ±10 %, and ±15 %, as well as the prediction errors (RMSE and MAE) of the four models, are summarized in Table 8. All four deep learning models have better relative humidity prediction performance than EPW which under predicts the relative humidity. However, all four models under predict the local relative humidity. Echoing the findings of temperature prediction, SP-P and SP-S models exhibit substantially diminished prediction errors compared to the LSTM and LSTM-M models. With the exception of accuracy within ±15 %, SP-S demonstrates superior performance. This comparative analysis underscores that building

**Table 5**  
Basic information for sensors on the microclimate station.

Metrics	Equation	Description
The root mean squared error (RMSE)	$\sqrt{\frac{1}{n} \sum_{i=1}^n (y_i - \hat{y}_i)^2}$	where n represents the number of samples, $y_i$ represents the observed value of the ith sample and $\hat{y}_i$ represents the predicted value of the ith sample
The mean absolute error (MAE)	$\frac{1}{n} \sum_{i=1}^n  y_i - \hat{y}_i $	where n represents the number of samples, $y_i$ represents the observed value of the ith sample and $\hat{y}_i$ represents the predicted value of the ith sample
The over-prediction ratio (OPR)	$\frac{\sum_{i=1}^n N_i}{n}$	where n represents the number of samples, $N_i$ is the counting index and $N_i = \begin{cases} 1 & \text{if } y_i - \hat{y}_i < 0 \\ 0 & \text{if } y_i - \hat{y}_i \geq 0 \end{cases}, y_i$ represents the observed value of the ith sample and $\hat{y}_i$ represents the predicted value of the ith sample where n represents the number of samples, $N_i$ is the counting index and $N_i = \begin{cases} 1 & \text{if }  y_i - \hat{y}_i  \leq 1 \\ 0 & \text{if }  y_i - \hat{y}_i  > 1 \end{cases}, y_i$ represents the observed value of the ith sample and $\hat{y}_i$ represents the predicted value of the ith sample where n represents the number of samples, $N_i$ is the counting index and $N_i = \begin{cases} 1 & \text{if }  y_i - \hat{y}_i  \leq 2 \\ 0 & \text{if }  y_i - \hat{y}_i  > 2 \end{cases}, y_i$ represents the observed value of the ith sample and $\hat{y}_i$ represents the predicted value of the ith sample where n represents the number of samples, $N_i$ is the counting index and $N_i = \begin{cases} 1 & \text{if }  y_i - \hat{y}_i  \leq 3 \\ 0 & \text{if }  y_i - \hat{y}_i  > 3 \end{cases}, y_i$ represents the observed value of the ith sample and $\hat{y}_i$ represents the predicted value of the ith sample where n represents the number of samples, $N_i$ is the counting index and $N_i = \begin{cases} 1 & \text{if }  y_i - \hat{y}_i  \leq 5 \\ 0 & \text{if }  y_i - \hat{y}_i  > 5 \end{cases}, y_i$ represents the observed value of the ith sample and $\hat{y}_i$ represents the predicted value of the ith sample where n represents the number of samples, $N_i$ is the counting index and $N_i = \begin{cases} 1 & \text{if }  y_i - \hat{y}_i  \leq 10 \\ 0 & \text{if }  y_i - \hat{y}_i  > 10 \end{cases}, y_i$ represents the observed value of the ith sample and $\hat{y}_i$ represents the predicted value of the ith sample where n represents the number of samples, $N_i$ is the counting index and $N_i = \begin{cases} 1 & \text{if }  y_i - \hat{y}_i  \leq 15 \\ 0 & \text{if }  y_i - \hat{y}_i  > 15 \end{cases}, y_i$ represents the observed value of the ith sample and $\hat{y}_i$ represents the predicted value of the ith sample
The temperature prediction accuracy within ±1 °C (± 1°C)	$\frac{\sum_{i=1}^n N_i}{n}$	
The temperature prediction accuracy within ±2 °C (± 2°C)	$\frac{\sum_{i=1}^n N_i}{n}$	
The temperature prediction accuracy within ±3 °C (± 3°C)	$\frac{\sum_{i=1}^n N_i}{n}$	
The relative humidity accuracy within ±5 % (± 5 %)	$\frac{\sum_{i=1}^n N_i}{n}$	
The relative humidity accuracy within ±10 % (± 10 %)	$\frac{\sum_{i=1}^n N_i}{n}$	
The relative humidity accuracy within ±15 % (± 15 %)	$\frac{\sum_{i=1}^n N_i}{n}$	

morphologies aligned with the sun path exhibit a stronger correlation with microclimate conditions than static 2D or 3D morphological factors.

Fig. 10 provides a comparative analysis of the actual relative humidity and the prediction outputs of the models on a typical day. During the early morning hours from 0:00 to 8:00, the three deep learning models with morphological inputs exhibit similar performance and outperform the LSTM model, except at 0:00 and 1:00. Subsequently, between 9:00 and 20:00, the prediction performances of SP-P and SP-S are better than those of the LSTM and LSTM-M models. However, during the time frame of 14:00 to 15:00, SP-P and SP-S show significant

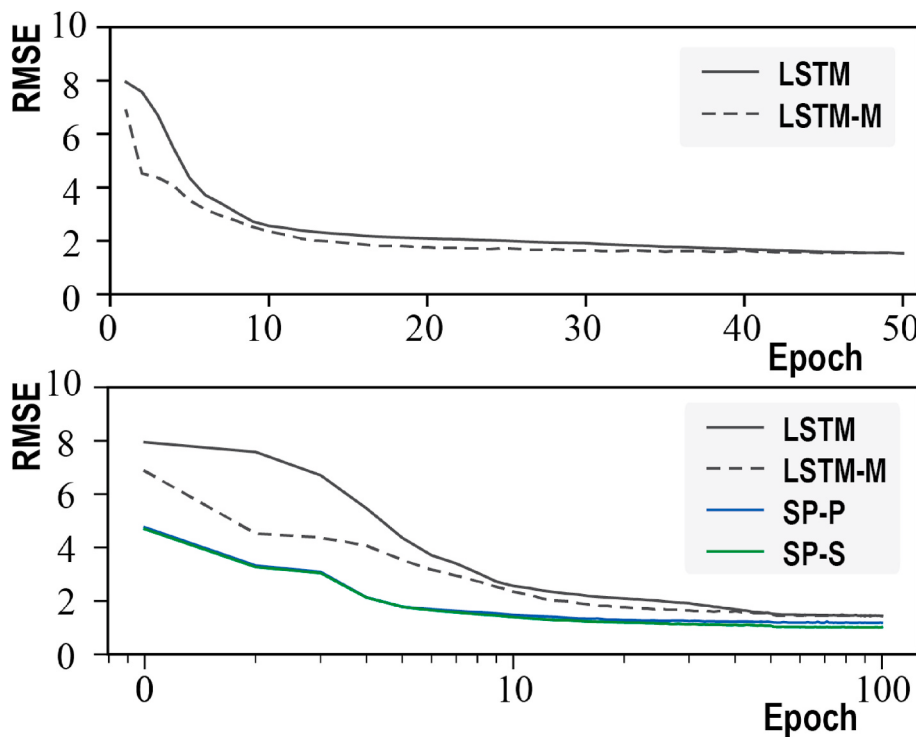


**Fig. 7.** The training errors of 4 deep learning models for temperature prediction.

**Table 6**  
The temperature prediction accuracy and errors.

	Acc $\pm 1$ °C	Acc $\pm 2$ °C	Acc $\pm 3$ °C	RMSE	MAE	OPR
EPW	5.5 %	12.5 %	23.1 %	6.765	2.432	29.5 %
LSTM	57.6 %	73.1 %	80.7 %	2.564	1.608	52.4 %
LSTM-M	59.8 %	75.5 %	83.5 %	2.212	1.432	63.7 %
SP-P	73.0 %	87.4 %	94.7 %	1.483	0.896	57.0 %
SP-S	72.4 %	86.1 %	94.4 %	1.551	0.944	59.5 %

prediction errors. As shown in Table 9, during the daytime, SP-P and SP-S achieve higher accuracy than LSTM and LSTM-M, with slight under-prediction. In summary, the integration of sun path-dependent transferred morphological features has the remarkable potential to greatly

enhance microclimate prediction.

### 5.3. Explanation of models' performance by morphological factors

The case study area encompasses 16 experimental sites characterized

**Table 7**

The temperature prediction accuracy and errors in the daytime.

	Acc $\pm 1$ °C	Acc $\pm 2$ °C	Acc $\pm 3$ °C	RMSE	MAE	OPR
LSTM	35.4 %	54.8 %	66.7 %	3.546	1.594	44.3 %
LSTM-M	39.3 %	58.7 %	71.6 %	3.003	1.470	50.9 %
SP-P	54.6 %	76.3 %	87.5 %	2.163	1.206	54.0 %
SP-S	54.1 %	78.7 %	87.8 %	2.080	1.184	52.4 %

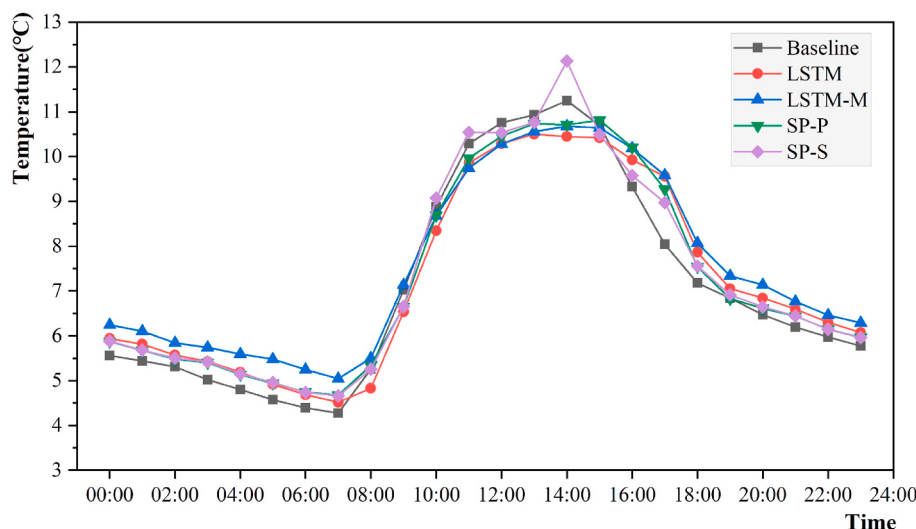


**Fig. 8.** The actual temperature and the predicted values by four deep learning models on a typical day.

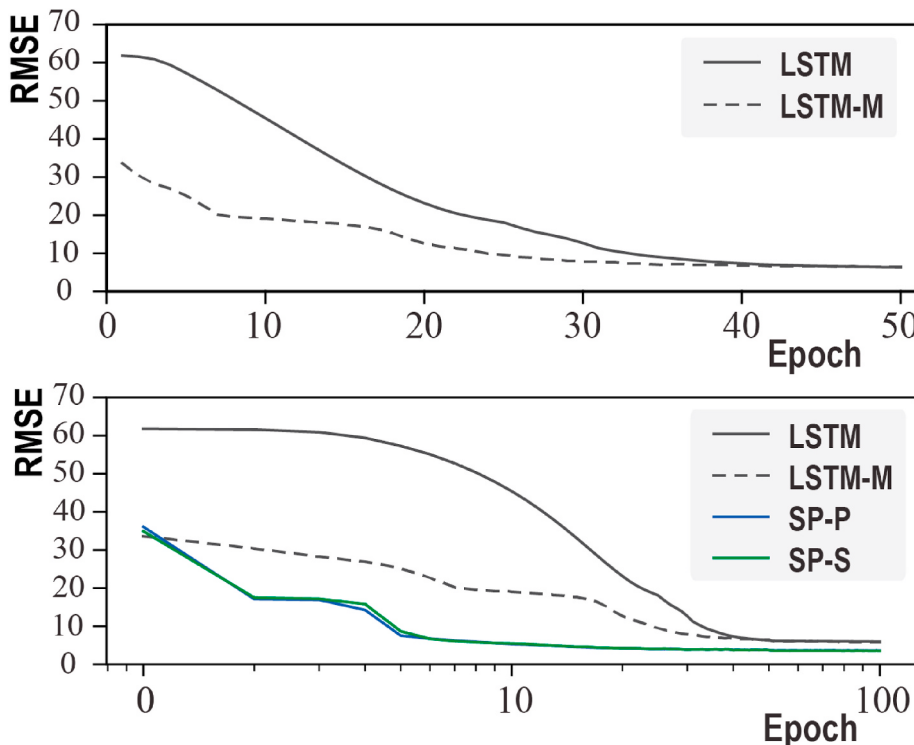


**Fig. 9.** The training errors of 4 deep learning models for relative humidity prediction.

**Table 8**  
The relative humidity prediction accuracy and errors.

	Acc ± 5 %	Acc ± 10 %	Acc ± 15 %	RMSE	MAE	OPR
EPW	12.6 %	23.0 %	37.7 %	24.165	4.523	39.3 %
LSTM	57.2 %	81.7 %	91.9 %	8.705	6.002	37.2 %
LSTM-M	63.9 %	86.7 %	94.5 %	7.814	5.159	40.2 %
SP-P	78.7 %	95.1 %	98.9 %	4.630	3.314	37.0 %
SP-S	80.3 %	95.7 %	98.7 %	4.536	3.175	31.8 %

by diverse landscapes influenced by buildings. To delve into the practicality of the two sun-path-dependent models, **Table 10** outlines the 11 static morphological factors for each experimental site. By pinpointing sites exhibiting lower RMSE values for the two models, the resemblance

in morphological factors can aid in identifying the most promising scenarios for the incorporation of frontal area matrixes. Concurrently, the RMSE discrepancy between the two sun-path-dependent models can offer insights into the optimal projection method for generating frontal area matrixes.

**Table 9**  
The relative humidity prediction accuracy and errors in the daytime.

	Acc ± 5 %	Acc ± 10 %	Acc ± 15 %	RMSE	MAE	OPR
LSTM	38.7 %	72.0 %	87.1 %	10.701	2.835	37.9 %
LSTM-M	47.6 %	75.6 %	88.6 %	10.430	2.694	41.6 %
SP-P	66.8 %	91.8 %	97.2 %	5.887	2.085	41.5 %
SP-S	65.7 %	90.6 %	97.8 %	5.896	2.101	37.1 %

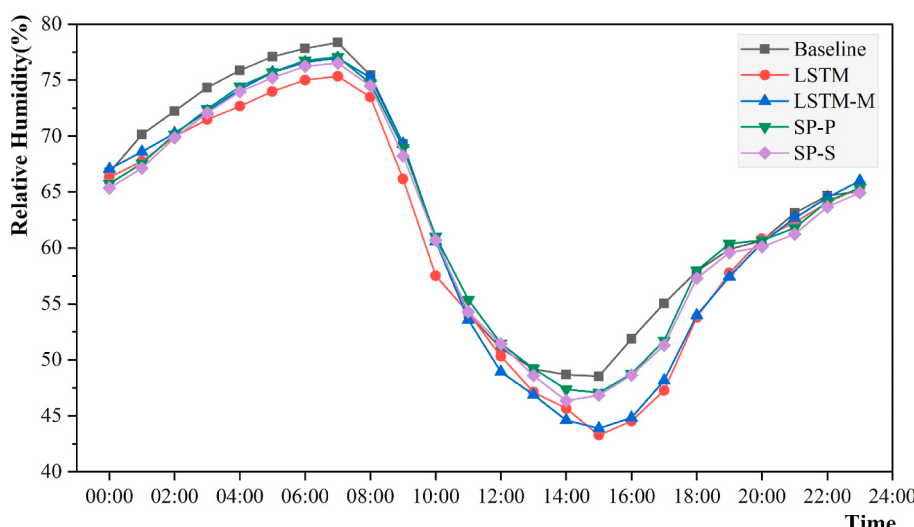


**Fig. 10.** The actual relative humidity and the predicted values by 4 deep learning models on a typical day.

**Table 10**

Static morphological factors at 16 experiment sites.

	PLAND	PAR	CV	PD	LPI	BVD	BHR	BO	BSA	BHD	HBI
S1	0.16	1273.9	0.99	3e-4	0.16	3.51	12.0	0.33	6.7e3	4.6e-3	0.67
S2	0.00	0.0	0.00	0.0	0.00	0.00	0.0	0.00	0.0	0.0	0.00
S3	0.16	0.0	0.00	1e-4	0.16	3.79	0.0	0.00	8.0e3	3.1e-3	1.00
S4	0.25	1342.1	0.83	4e-4	0.17	3.55	6.0	0.18	9.0e3	6.1e-3	0.42
S5	0.18	0.0	0.00	1e-4	0.18	3.73	0.0	0.00	6.6e3	2.7e-3	1.00
S6	0.41	1338.8	0.62	5e-4	0.21	6.13	17.0	0.66	1.4e4	5.7e-3	0.47
S7	0.25	1717.8	1.19	4e-4	0.22	4.14	8.2	0.21	9.4e3	6.2e-3	0.41
S8	0.35	799.0	0.63	9e-4	0.11	4.21	11.8	0.38	1.2e4	1.0e-2	0.21
S9	0.37	1731.2	1.20	6e-4	0.22	7.46	39.0	0.63	1.6e4	1.3e-2	0.43
S10	0.29	650.3	0.40	5e-4	0.12	6.52	44.0	0.68	1.5e4	1.2e-2	0.54
S11	0.33	490.6	0.31	5e-4	0.11	5.55	44.5	0.80	1.2e4	1.1e-2	0.59
S12	0.15	535.9	0.64	5e-4	0.08	2.07	12.6	0.40	6.6e3	6.7e-3	0.32
S13	0.35	814.9	0.45	5e-4	0.16	1.69	4.0	0.35	8.1e3	2.5e-3	0.40
S14	0.38	1199.8	1.12	1.1e-3	0.15	8.07	17.0	0.35	1.9e4	2.1e-2	0.15
S15	0.46	1927.4	1.08	8e-4	0.25	10.31	12.0	0.21	2.0e4	1.6e-2	0.19
S16	0.45	1889.0	0.98	6e-4	0.24	8.69	12.0	0.27	1.7e4	1.1e-2	0.28

As illustrated in Fig. 11, both SP-P and SP-S exhibit comparable enhancements in temperature prediction errors across most sites. Notably, a significant improvement is evident at S1, S7, S9, and S10,

where the RMSE demonstrates reductions exceeding 2 °C and 1 °C in comparison to LSTM and LSTM-M, respectively. In these specific sites, PLAND values (below 0.4) and PD values (below 6e-4) are notably low,

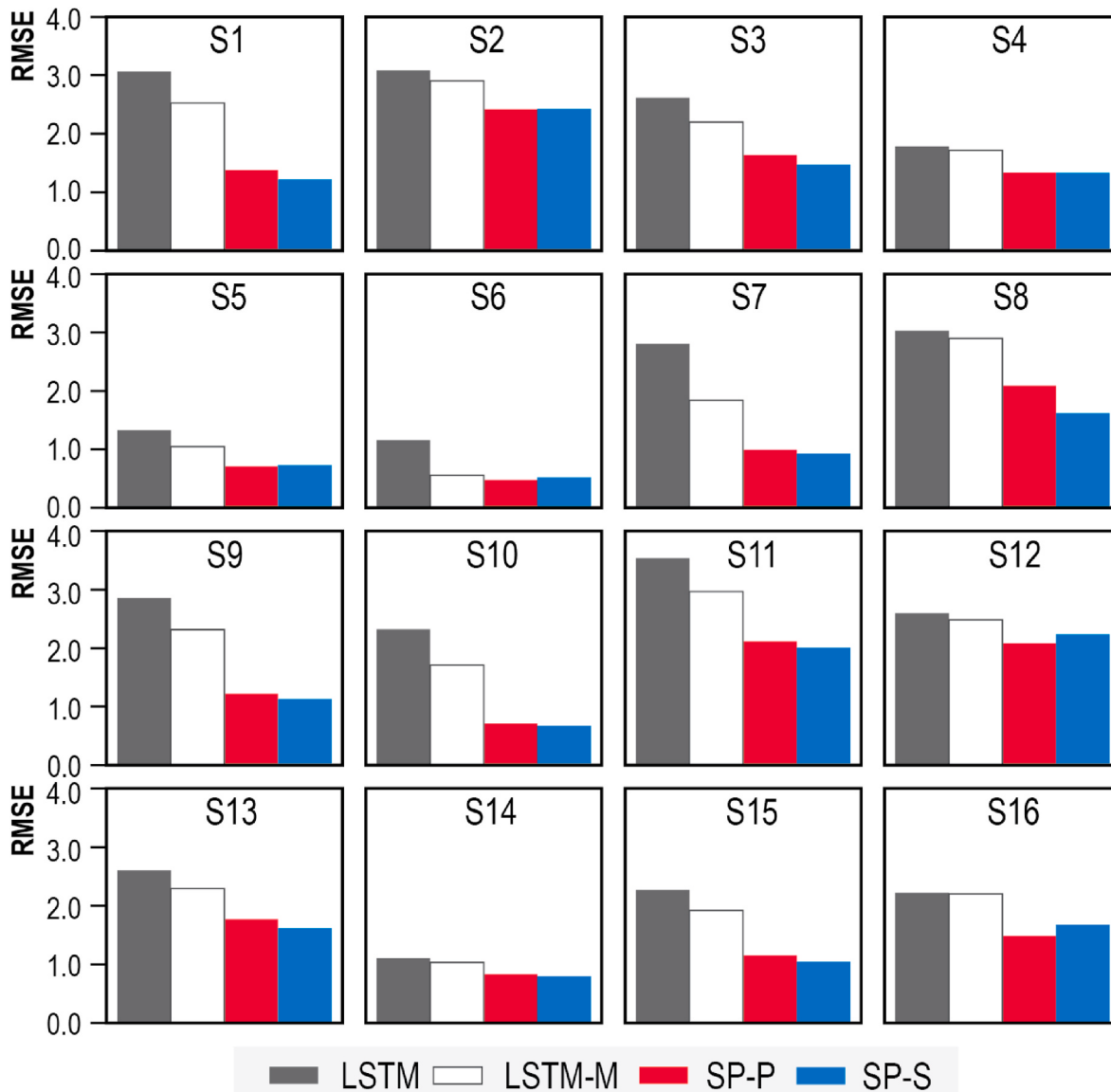


Fig. 11. Prediction errors of temperature at 16 experiment sites.

indicating a diminutive 2D footprint of the buildings. Additionally, the elevated HBI values (above 0.4) are indicative of substantial construction. The SP-P model outperforms SP-S at S2, S5, S6, S12, and S16, with particularly pronounced results observed at S12 and S16, featuring RMSE differences exceeding 0.15. Notably, BHR values (around 12) at these locations are exceptionally high. Consequently, the parallel projection matrix proves more suitable for areas with vertical disparities in shape, while the surround projection matrix proves more efficacious in regions characterized by comparable building heights.

The comparison of relative humidity errors is depicted in Fig. 12, showcasing the similar prediction errors of SP-P and SP-S models. These two models exhibit noteworthy RMSE reductions of over 5 % in comparison to LSTM and LSTM-M at S7, S10, S11, and S13. Within these sites, moderate PLAND values (approximately 0.3) and HBI values (around 0.5) are discerned, indicating a relatively uniform building shape. The lowest RMSE is achieved by SP-P at S4, S7, S8, S11, S12, and S16. Notably, a substantial RMSE disparity of approximately 0.2 is evident between SP-P and SP-S at S7 and S12, sites characterized by relatively low PLAND values. Consequently, the parallel projection method proves more effective in areas with sparse building density, while the surround projection method demonstrates better performance in handling regions with high-density building clusters.

Deep learning methods excel in handling intricate latent connections, yet their intricate computational processes hinder interpretability. To discern the relative significance of distinct morphological features and stimulate innovative approaches for morphology characterization, this study incorporates Spearman rank correlation analysis based on prediction RMSE. The Spearman rank correlation coefficient ( $\rho_T$  and  $\rho_H$ ) along with associated probability values (p-values) are compiled in Table 11. Notably, all 11 factors exhibit negative correlations with RMSE for both SP-P and SP-S. LPI, BVD, and BSA exhibit noteworthy correlations with temperature prediction (p-value  $<0.05$ ), indicating enhanced performance in locales with substantial buildings spanning both horizontal and vertical dimensions. Regarding relative humidity, LPI and BSA exhibit significance for SP-P (p-value  $<0.05$ ), while solely LPI emerges as significant for SP-S (p-value  $<0.05$ ). Consequently, 2D morphological features emerge as pivotal in relative humidity prediction.

## 6. Discussion

This study introduces two projection methodologies for generating binary 2D frontal area matrices in varying orientations. In contrast to conventional static building morphological factors, the approach selects

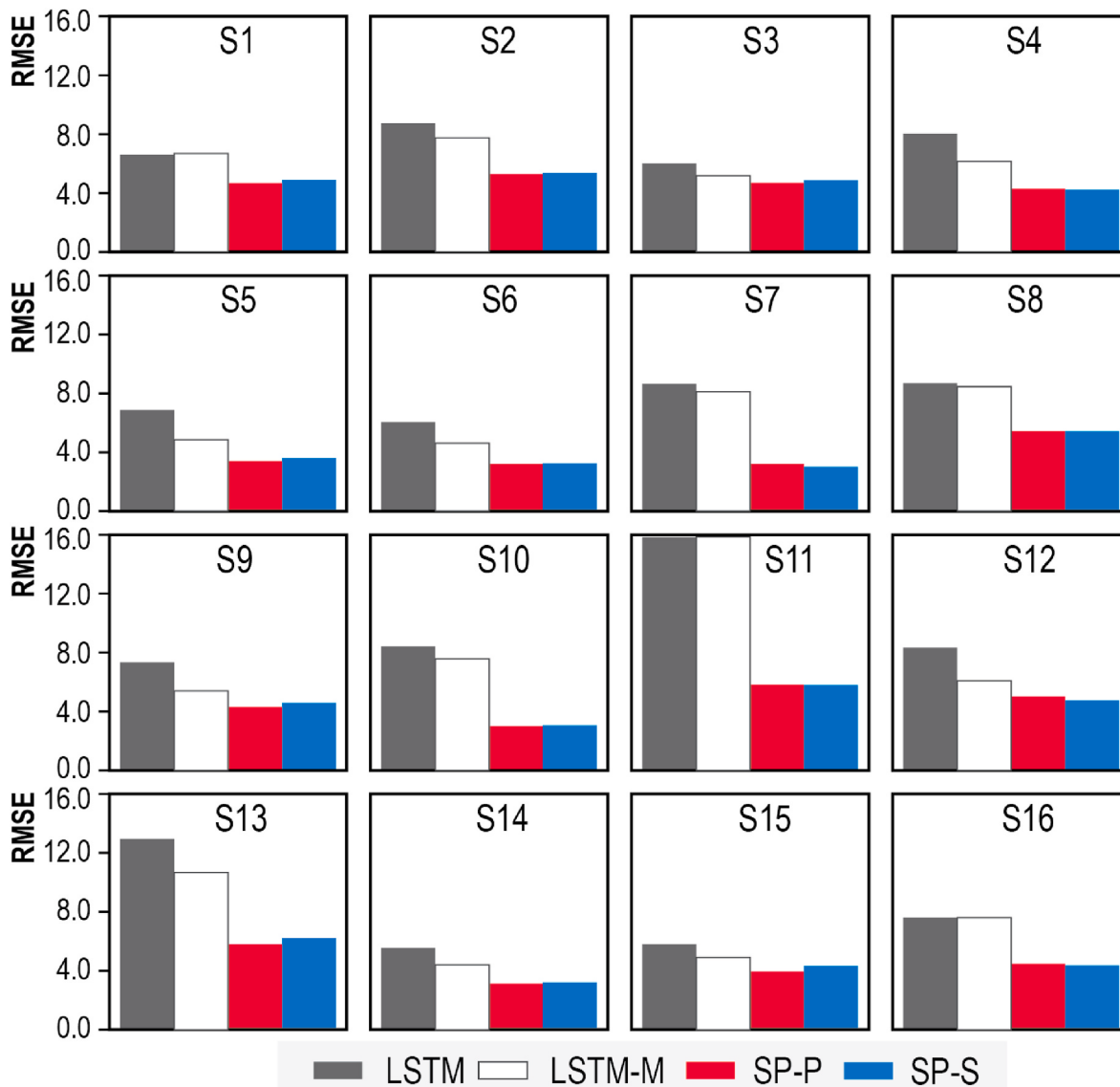


Fig. 12. Prediction errors of relative humidity at 16 experiment sites.

**Table 11**  
Spearman rank correlation coefficients of morphology factors.

	SP-P				SP-S			
	$\rho_T$	p-value	$\rho_H$	p-value	$\rho_T$	p-value	$\rho_H$	p-value
PLAND	-0.359	4.7e-06	-0.282	5.9e-11	-0.341	7.4e-06	-0.197	6.6e-11
PAR	-0.351	3.1e-05	-0.354	3.2e-05	-0.277	3.1e-05	-0.342	3.2e-05
CV	-0.283	2.5e-03	-0.339	2.0e-09	-0.230	4.1e-03	-0.348	2.2e-09
PD	-0.100	8.3e-08	-0.123	1.4e-11	-0.100	1.1e-07	-0.075	1.7e-11
LPI	-0.579	9.6e-07	-0.462	3.7e-11	-0.488	1.3e-06	-0.444	4.3e-11
BVD	-0.459	3.5e-04	-0.497	4.8e-01	-0.432	2.9e-04	-0.450	5.4e-01
BHR	-0.211	2.3e-03	-0.244	1.2e-02	-0.220	2.2e-03	-0.202	1.2e-02
BO	-0.044	1.2e-05	-0.003	7.0e-11	-0.106	2.0e-05	0.047	8.7e-11
BSA	-0.409	6.4e-07	-0.444	6.4e-07	-0.406	6.4e-07	-0.379	6.4e-07
BHD	-0.238	9.3e-08	-0.350	1.4e-11	-0.224	1.2e-07	-0.338	1.8e-11
HBI	-0.278	8.0e-05	-0.079	1.8e-10	-0.331	1.4e-04	-0.050	1.8e-10

an effective frontal area slice that captures buildings' shading impact based on sun path variation. Deep transfer learning neural networks were formulated to compute environment-related morphological attributes, thereby enhancing the precision of microclimate condition predictions. Two sun-path-dependent models were devised, employing distinct projection matrices, and their prediction accuracy was benchmarked against the LSTM and LSTM-M models. The final outcomes underscore that both SP-P and SP-S models yield noteworthy enhancements in microclimate prediction. Spearman analysis of morphological factors underscores that temperature prediction is influenced by both 2D and 3D morphological features, while 2D characteristics primarily shape relative humidity prediction.

The assessment of urban air and heat convection heavily relies on buildings' frontal area, a pivotal factor [17]. Traditional methods of calculating the frontal area index tend to focus on cumulative or incremental façade areas along each wind direction [44,45,61,62]. However, these generalized approaches lead to a significant loss of geometric characteristics, resulting in a weak correlation between the built environment and climatic conditions [46]. Moreover, the abstracted frontal area index offers limited potential for subsequent feature extraction. The proposed projection techniques expand frontal area computations by generating graph-like data. Binary 2D matrices succinctly capture the distribution and obstructive aspects of building façades. Consequently, the open area arrangement within the 2D matrix offers a robust assessment of buildings' shading effects within microclimate zones [63]. Additionally, graph-like data optimally leverage the capabilities of deep transfer learning neural networks by furnishing ample features.

The two frontal area projection methods present a novel approach to quantify the impact of solar radiation on local microclimate conditions. The facades of buildings that face the incoming sunlight create shadows, playing a central role in shaping the urban thermal environment [64]. However, the climatic effect of shadows remains closely tied to morphological features, and Bourbia and Awbi have suggested that changes in shadow do not significantly affect air temperature [65]. Based on the concept of interactions between buildings, this study transforms these façades into a 2D matrix that captures the interplay between solar radiation and the surrounding structures.

The development of a sun-path-dependent 2D matrix for the frontal area has far-reaching implications for existing theories in urban environmental analysis. Prior efforts have predominantly concentrated on the direct impacts of the built environment on microclimate. However, these effects can be influenced by the indirect interplay between building morphology and the natural environment (sun path, wind direction, and cloud cover). Extracting meaningful features from static building morphologies can effectively elucidate variations in microclimate conditions. Moreover, morphological factors could be aligned with various climate parameters or air pollutants. This approach may unveil the concealed mechanisms of morphological effects, contributing to assessing the UHI effect and enriching our understanding of air quality. For urban planners and administrators, an expanded array of indices can

offer insights into daily or seasonal morphological effects. Additionally, building upon these indices could lead to more precise and valuable strategies for city energy provision and public health advisories.

However, the proposed sun-path-dependent methods with 2D matrix inputs do have some limitations. First, this study concentrates on the shading effect of building facades, while rooftops can also obstruct solar radiation and cast shadows. Hence, the morphological features of building roofs should also be integrated with the sun path. Second, it's imperative to delve into the seasonal fluctuations of microclimate conditions. Solar azimuth and zenith exhibit periodic changes throughout the year, resulting in variations in irradiation. Given that this case study was conducted in winter, the performance of deep transfer learning models should be assessed in other seasons. In this study, the test period was limited, which prevented the inclusion of the full variation of the solar path throughout the entire year. As a result, the model's performance could only be validated for a specific period. However, it is important to note that each season exhibits a distinct range of solar azimuth and zenith angles, and this aspect requires further investigation with an ample amount of data. In future research, the validation test will be extended to include a longer data collection period, ideally spanning over one year, to provide more comprehensive insights and validate the model's performance across different seasons. Third, exploring the size of the microclimate zone is crucial to account for buildings with limited climate influence. While this study involves buildings within a 50-m radius of data collection points for morphological calculation, buildings beyond this radius could still have significance. Then, this study assumes that the built environment is relatively stable over long periods. However, in reality, destructions and new constructions can occur due to rapid urbanization. Therefore, it is important to collect and update up-to-date building morphology information before using the proposed method. Lastly, the model's robustness should be examined across different climatic regions, and the climate's impact on building shading must be carefully scrutinized.

## 7. Conclusion

Weather data constitutes a crucial parameter that greatly impacts the accuracy of city-scale building energy simulations. However, traditional simulation methods rely on uniform TMY files for the entire city, overlooking the variability in local microclimate conditions. In response, this study introduces two projection methods to deconstruct the frontal area of surrounding structures into binary 2D matrices. These features serve as inputs for sun path-dependent deep transfer learning neural networks, aimed at predicting microclimate patterns. A validation experiment was executed to gather local microclimate data via a wireless sensor system. The results of the experiment underscore the effectiveness of the proposed methodologies in enhancing microclimate prediction accuracy. Specifically, SP-P and SP-S yield superior outcomes in temperature and relative humidity prediction, respectively.

## CRediT authorship contribution statement

**Qi Li:** Writing – original draft, Visualization, Validation, Methodology, Investigation, Formal analysis. **Wei Wang:** Validation, Resources, Investigation, Data curation. **Xiaowei Luo:** Validation, Resources. **Jiayu Chen:** Writing – review & editing, Project administration, Methodology, Funding acquisition.

## Declaration of competing interest

The authors declare that they have no known competing financial interests or personal relationships that could have appeared to influence the work reported in this paper.

## Data availability

The data that has been used is confidential.

## Acknowledgement

This work was financially supported by the Talent Introduction Fund of Tsinghua University, #53331400223. Any opinions, findings, conclusions, or recommendations expressed in this paper are those of the authors and do not necessarily reflect the views of Tsinghua University.

## References

- [1] H. Wang, W. Chen, J. Shi, Low carbon transition of global building sector under 2- and 1.5-degree targets, *Appl. Energy* 222 (2018) 148–157, <https://doi.org/10.1016/j.apenergy.2018.03.090>.
- [2] Z. Long, M. Zhong, Experimental study on the vertical temperature and thermal stratification for subway station fire, *J. Intell. Constr.* (2023), <https://doi.org/10.26599/JIC.2023.9180030>.
- [3] J. Zhang, Z. Li, Y. Wei, D. Hu, The impact of the building morphology on microclimate and thermal comfort-a case study in Beijing, *Build. Environ.* 223 (2022) 109469, <https://doi.org/10.1016/j.buildenv.2022.109469>.
- [4] H. Wang, W. Chen, J. Shi, Low carbon transition of global building sector under 2- and 1.5-degree targets, *Appl. Energy* 222 (2018) 148–157, <https://doi.org/10.1016/j.apenergy.2018.03.090>.
- [5] D. Han, X. Xu, Z. Qiao, F. Wang, H. Cai, H. An, K. Jia, Y. Liu, Z. Sun, S. Wang, W. Han, The roles of surrounding 2D/3D landscapes in park cooling effect: analysis from extreme hot and normal weather perspectives, *Build. Environ.* 231 (2023) 110053, <https://doi.org/10.1016/j.buildenv.2023.110053>.
- [6] Y. Xiang, P. Lin, R. An, J. Yuan, Q. Fan, X. Chen, Full participation flat closed-loop safety management method for offshore wind power construction sites, *J. Intell. Constr.* 1 (2023) 918006, <https://doi.org/10.26599/jic.2023.918006>.
- [7] M. Zhang, X. Zhang, S. Guo, X. Xu, J. Chen, W. Wang, Urban micro-climate prediction through long short-term memory network with long-term monitoring for on-site building energy estimation, *Sustain. Cities Soc.* 74 (2021) 103227, <https://doi.org/10.1016/j.scs.2021.103227>.
- [8] R. Ma, B. Ren, D. Zhao, J. Chen, Y. Lu, Modeling urban energy dynamics under clustered urban heat island effect with local-weather extended distributed adjacency blocks, *Sustain. Cities Soc.* 56 (2020) 102099, <https://doi.org/10.1016/j.scs.2020.102099>.
- [9] B. Zhao, R.-Q. Wang, S. Cao, Modeling the cleaning cycle dynamics for air cooling condensers of thermal power plants: optimization and global sensitivity analysis, *J. Intell. Constr.* 1 (2023) 9180023, <https://doi.org/10.26599/jic.2023.9180023>.
- [10] T. Hong, Y. Xu, K. Sun, W. Zhang, X. Luo, B. Hooper, Urban microclimate and its impact on building performance: a case study of San Francisco, *Urban Clim.* 38 (2021) 100871, <https://doi.org/10.1016/j.uclim.2021.100871>.
- [11] L. Xu, S. Tong, W. He, W. Zhu, S. Mei, K. Cao, C. Yuan, Better understanding on impact of microclimate information on building energy modelling performance for urban resilience, *Sustain. Cities Soc.* 80 (2022) 103775, <https://doi.org/10.1016/j.scs.2022.103775>.
- [12] R. Ma, T. Wang, Y. Wang, J. Chen, Tuning urban microclimate: a morpho-patch approach for multi-scale building group energy simulation, *Sustain. Cities Soc.* 76 (2022) 103516, <https://doi.org/10.1016/j.scs.2021.103516>.
- [13] Y. Li, W. Ouyang, S. Yin, Z. Tan, C. Ren, Microclimate and its influencing factors in residential public spaces during heat waves: an empirical study in Hong Kong, *Build. Environ.* 236 (2023) 110225, <https://doi.org/10.1016/j.buildenv.2023.110225>.
- [14] R. Ma, X. Li, J. Chen, An elastic urban morpho-blocks (EUM) modeling method for urban building morphological analysis and feature clustering, *Build. Environ.* 192 (2021) 107646, <https://doi.org/10.1016/j.buildenv.2021.107646>.
- [15] Z. Wu, P. Dou, L. Chen, Comparative and combinative cooling effects of different spatial arrangements of buildings and trees on microclimate, *Sustain. Cities Soc.* 51 (2019) 101711, <https://doi.org/10.1016/j.scs.2019.101711>.
- [16] X. He, W. Gao, R. Wang, Impact of urban morphology on the microclimate around elementary schools: a case study from Japan, *Build. Environ.* 206 (2021) 108383, <https://doi.org/10.1016/j.buildenv.2021.108383>.
- [17] H. Li, Y. Li, T. Wang, Z. Wang, M. Gao, H. Shen, Quantifying 3D building form effects on urban land surface temperature and modeling seasonal correlation patterns, *Build. Environ.* 204 (2021) 108132, <https://doi.org/10.1016/j.buildenv.2021.108132>.
- [18] Y. Xu, C. Ren, P. Ma, J. Ho, W. Wang, K.K.L. Lau, H. Lin, E. Ng, Urban morphology detection and computation for urban climate research, *Landscape. Urban Plan.* 167 (2017) 212–224, <https://doi.org/10.1016/j.landurbplan.2017.06.018>.
- [19] X. Du, R. Bokel, A. van den Dobbelsteen, Building microclimate and summer thermal comfort in free-running buildings with diverse spaces: a Chinese vernacular house case, *Build. Environ.* 82 (2014) 215–227, <https://doi.org/10.1016/j.buildenv.2014.08.022>.
- [20] H. Ye, X. Hu, Q. Ren, T. Lin, X. Li, G. Zhang, L. Shi, Effect of urban micro-climatic regulation ability on public building energy usage carbon emission, *Energy Build.* 154 (2017) 553–559, <https://doi.org/10.1016/j.enbuild.2017.08.047>.
- [21] Y. Dong, J. Yuan, Projections of offshore wind energy and wave climate in Guangdong's nearshore area using CMIP6 simulations, *J. Intell. Constr.* 1 (2023) 9180007, <https://doi.org/10.26599/jic.2023.9180007>.
- [22] P. Zhang, N. Xu, P. Xiao, T. Zhao, F. Gao, X. Ding, B. Li, Microseismic source location based on improved artificial bee colony algorithm: performance analysis and case study, *J. Intell. Constr.* 1 (2023) 9180016, <https://doi.org/10.26599/jic.2023.9180016>.
- [23] F. Peng, Y. Xiong, B. Zou, Identifying the optimal travel path based on shading effect at pedestrian level in cool and hot climates, *Urban Clim.* 40 (2021) 100988, <https://doi.org/10.1016/j.uclim.2021.100988>.
- [24] N. Nasrullahi, Y. Namazi, M. Taleghani, The effect of urban shading and canyon geometry on outdoor thermal comfort in hot climates: a case study of Ahvaz, Iran, *Sustain. Cities Soc.* 65 (2021) 102638, <https://doi.org/10.1016/j.scs.2020.102638>.
- [25] J.A. Rodríguez Algeciras, A. Matzarakis, Quantification of thermal bioclimate for the management of urban design in Mediterranean climate of Barcelona, Spain, *Int. J. Biometeorol.* 60 (2016) 1261–1270, <https://doi.org/10.1007/s00484-015-1121-8>.
- [26] A.M. Elmalky, M.T. Araji, Computational procedure of solar irradiation: a new approach for high performance façades with experimental validation, *Energy Build.* 298 (2023), <https://doi.org/10.1016/j.enbuild.2023.113491>.
- [27] J. Rodríguez-Algeciras, A. Tablada, A. Matzarakis, Effect of asymmetrical street canyons on pedestrian thermal comfort in warm-humid climate of Cuba, *Theor. Appl. Climatol.* 133 (2018) 663–679, <https://doi.org/10.1007/s00704-017-2204-8>.
- [28] K.M. Wai, C. Yuan, A. Lai, P.K.N. Yu, Relationship between pedestrian-level outdoor thermal comfort and building morphology in a high-density city, *Sci. Total Environ.* 708 (2020) 134516, <https://doi.org/10.1016/j.scitotenv.2019.134516>.
- [29] K. Perini, A. Magliocco, Effects of vegetation, urban density, building height, and atmospheric conditions on local temperatures and thermal comfort, *Urban For. Urban Green.* 13 (2014) 495–506, <https://doi.org/10.1016/j.ufug.2014.03.003>.
- [30] J. Brozovsky, J. Radivojevic, A. Simonsen, Assessing the impact of urban microclimate on building energy demand by coupling CFD and building performance simulation, *J. Build. Eng.* 55 (2022) 104681, <https://doi.org/10.1016/j.jobe.2022.104681>.
- [31] T. Sharmin, K. Steemers, A. Matzarakis, Microclimatic modelling in assessing the impact of urban geometry on urban thermal environment, *Sustain. Cities Soc.* 34 (2017) 293–308, <https://doi.org/10.1016/j.scs.2017.07.006>.
- [32] X. He, S. Miao, S. Shen, J. Li, B. Zhang, Z. Zhang, X. Chen, Influence of sky view factor on outdoor thermal environment and physiological equivalent temperature, *Int. J. Biometeorol.* 59 (2015) 285–297, <https://doi.org/10.1007/s00484-014-0841-5>.
- [33] Y. Wang, H. Akbari, Analysis of urban heat island phenomenon and mitigation solutions evaluation for Montreal, *Sustain. Cities Soc.* 26 (2016) 438–446, <https://doi.org/10.1016/j.scs.2016.04.015>.
- [34] A.S. Jihad, M. Tahiri, Modeling the urban geometry influence on outdoor thermal comfort in the case of Moroccan microclimate, *Urban Clim.* 16 (2016) 25–42, <https://doi.org/10.1016/j.uclim.2016.02.002>.
- [35] S. Chen, W. Zhang, N.H. Wong, M. Ignatius, Combining CityGML files and data-driven models for microclimate simulations in a tropical city, *Build. Environ.* 185 (2020) 107314, <https://doi.org/10.1016/j.buildenv.2020.107314>.
- [36] H. Yang, G. Chen, D. Wang, J. Hang, Q. Li, Q. Wang, Influences of street aspect ratios and realistic solar heating on convective heat transfer and ventilation in full-scale 2D street canyons, *Build. Environ.* 204 (2021) 108125, <https://doi.org/10.1016/j.buildenv.2021.108125>.
- [37] J. Rhee, S. Park, Z. Lu, Relationship between land cover patterns and surface temperature in urban areas, *GIScience Remote Sens.* 51 (2014) 521–536, <https://doi.org/10.1080/15481603.2014.964455>.
- [38] J.P. Connors, C.S. Galletti, W.T.L. Chow, Landscape configuration and urban heat island effects: assessing the relationship between landscape characteristics and land surface temperature in Phoenix, Arizona, *Landscape. Ecol.* 28 (2013) 271–283, <https://doi.org/10.1007/s10980-012-9833-1>.
- [39] C. Yang, W. Zhu, J. Sun, X. Xu, R. Wang, Y. Lu, S. Zhang, W. Zhou, Assessing the effects of 2D/3D urban morphology on the 3D urban thermal environment by using multi-source remote sensing data and UAV measurements: a case study of the snow-climate city of Changchun, China, *J. Clean. Prod.* 321 (2021) 128956, <https://doi.org/10.1016/j.jclepro.2021.128956>.
- [40] Z. Li, D. Hu, Exploring the relationship between the 2D/3D architectural morphology and urban land surface temperature based on a boosted regression

- tree: a case study of Beijing, China, *Sustain. Cities Soc.* 78 (2022) 103392, <https://doi.org/10.1016/j.scs.2021.103392>.
- [41] S. Yu, Z. Chen, B. Yu, L. Wang, B. Wu, J. Wu, F. Zhao, Exploring the relationship between 2D/3D landscape pattern and land surface temperature based on explainable eXtreme Gradient Boosting tree: a case study of Shanghai, China, *Sci. Total Environ.* 725 (2020) 138229, <https://doi.org/10.1016/j.scitotenv.2020.138229>.
- [42] Y. Tian, W. Zhou, Y. Qian, Z. Zheng, J. Yan, The effect of urban 2D and 3D morphology on air temperature in residential neighborhoods, *Landscape Ecol.* 34 (2019) 1161–1178, <https://doi.org/10.1007/s10980-019-00834-7>.
- [43] F. Xu, Z. Gao, Frontal area index: a review of calculation methods and application in the urban environment, *Build. Environ.* 224 (2022) 109588, <https://doi.org/10.1016/j.buildenv.2022.109588>.
- [44] Z. Li, H. Zhang, C.Y. Wen, A.S. Yang, Y.H. Juan, Effects of frontal area density on outdoor thermal comfort and air quality, *Build. Environ.* 180 (2020) 107028, <https://doi.org/10.1016/j.buildenv.2020.107028>.
- [45] E. Ng, C. Yuan, L. Chen, C. Ren, J.C.H. Fung, Improving the wind environment in high-density cities by understanding urban morphology and surface roughness: a study in Hong Kong, *Landscape Urban Plan.* 101 (2011) 59–74, <https://doi.org/10.1016/j.landurbplan.2011.01.004>.
- [46] Y. Shi, X. Xie, J.C.H. Fung, E. Ng, Identifying critical building morphological design factors of street-level air pollution dispersion in high-density built environment using mobile monitoring, *Build. Environ.* 128 (2018) 248–259, <https://doi.org/10.1016/j.buildenv.2017.11.043>.
- [47] Q. Li, W. Wang, Z. Yu, J. Chen, Assessing urban micro-climates with vertical and horizontal building morphological cutting deep transfer learning neural networks, *Build. Environ.* 234 (2023) 110186, <https://doi.org/10.1016/j.buildenv.2023.110186>.
- [48] Z. Zhang, S. Zhang, Z. Zhao, L. Yan, C. Wang, H. Liu, HydroBIM—digital design, intelligent construction, and smart operation, *J. Intell. Constr.* 1 (2023) 9180014, <https://doi.org/10.26599/JIC.2023.9180014>.
- [49] P. Lin, J. Jia, J. Yuan, Journal of Intelligent Construction : a new platform for sharing multidisciplinary research on emerging construction technologies, *J. Intell. Constr.* 1 (2023) 9180008, <https://doi.org/10.26599/jic.2023.9180008>.
- [50] W. Xu, S. Guo, S. Yao, Structural stiffness evaluation of suspension bridge based on monitoring data, *J. Intell. Constr.* 1 (2023) 9180013, <https://doi.org/10.26599/jic.2023.9180013>.
- [51] Q. Li, J. Chen, X. Luo, Estimating omnidirectional urban vertical wind speed with direction-dependent building morphologies, *Energy Build.* 303 (2024) 113749, <https://doi.org/10.1016/j.enbuild.2023.113749>.
- [52] M. Kolokotroni, M. Davies, B. Croxford, S. Bhuiyan, A. Mavrogianni, A validated methodology for the prediction of heating and cooling energy demand for buildings within the Urban Heat Island: case-study of London, *Sol. Energy* 84 (2010) 2246–2255, <https://doi.org/10.1016/j.solener.2010.08.002>.
- [53] S. Ghimire, R.C. Deo, N.J. Downs, N. Raj, Global solar radiation prediction by ANN integrated with European Centre for medium range weather forecast fields in solar rich cities of Queensland Australia, *J. Clean. Prod.* 216 (2019) 288–310, <https://doi.org/10.1016/j.jclepro.2019.01.158>.
- [54] C. Fan, F. Xiao, Y. Zhao, A short-term building cooling load prediction method using deep learning algorithms, *Appl. Energy* 195 (2017) 222–233, <https://doi.org/10.1016/j.apenergy.2017.03.064>.
- [55] J.M. Han, Y.Q. Ang, A. Malkawi, H.W. Samuelson, Using recurrent neural networks for localized weather prediction with combined use of public airport data and on-site measurements, *Build. Environ.* 192 (2021) 107601, <https://doi.org/10.1016/j.buildenv.2021.107601>.
- [56] J. Ma, Z. Li, J.C.P. Cheng, Y. Ding, C. Lin, Z. Xu, Air quality prediction at new stations using spatially transferred bi-directional long short-term memory network, *Sci. Total Environ.* 705 (2020) 135771, <https://doi.org/10.1016/j.scitotenv.2019.135771>.
- [57] Q. Cao, Q. Luan, Y. Liu, R. Wang, The effects of 2D and 3D building morphology on urban environments: a multi-scale analysis in the Beijing metropolitan region, *Build. Environ.* 192 (2021) 107635, <https://doi.org/10.1016/j.buildenv.2021.107635>.
- [58] S. Tong, N.H. Wong, S.K. Jusuf, C.L. Tan, H.F. Wong, M. Ignatius, E. Tan, Study on correlation between air temperature and urban morphology parameters in built environment in northern China, *Build. Environ.* Times 127 (2018) 239–249, <https://doi.org/10.1016/j.buildenv.2017.11.013>.
- [59] S. Alavipanah, J. Schreyer, D. Haase, T. Lakes, S. Qureshi, The effect of multi-dimensional indicators on urban thermal conditions, *J. Clean. Prod.* 177 (2018) 115–123, <https://doi.org/10.1016/j.jclepro.2017.12.187>.
- [60] K. He, X. Zhang, S. Ren, J. Sun, Deep residual learning for image recognition, in: 2016 IEEE Conf. Comput. Vis. Pattern Recognit., IEEE, 2016, pp. 770–778, <https://doi.org/10.1109/CVPR.2016.90>.
- [61] M.S. Wong, J.E. Nichol, P.H. To, J. Wang, A simple method for designation of urban ventilation corridors and its application to urban heat island analysis, *Build. Environ.* 45 (2010) 1880–1889, <https://doi.org/10.1016/j.buildenv.2010.02.019>.
- [62] Y. Shi, K.K.L. Lau, E. Ng, Incorporating wind availability into land use regression modelling of air quality in mountainous high-density urban environment, *Environ. Res.* 157 (2017) 17–29, <https://doi.org/10.1016/j.envres.2017.05.007>.
- [63] J. Zhu, J. Feng, J. Lu, Y. Chen, W. Li, P. Lian, X. Zhao, A review of the influence of courtyard geometry and orientation on microclimate, *Build. Environ.* 236 (2023) 110269, <https://doi.org/10.1016/j.buildenv.2023.110269>.
- [64] S. Wonorahardjo, I.M. Sutjahja, Y. Mardiyati, H. Andoni, R.A. Achsani, S. Steven, D. Thomas, E. Tunçbilek, M. Arıcı, N. Rahmah, S. Tedja, Effect of different building façade systems on thermal comfort and urban heat island phenomenon: an experimental analysis, *Build. Environ.* 217 (2022) 109063, <https://doi.org/10.1016/j.buildenv.2022.109063>.
- [65] F. Bourbia, H.B. Awbi, Building cluster and shading in urban canyon for hot dry climate Part 1: air and surface temperature measurements, *Renew. Energy* 29 (2004) 249–262, [https://doi.org/10.1016/S0960-1481\(03\)00170-8](https://doi.org/10.1016/S0960-1481(03)00170-8).